

**ENERGY-BASED APPROACH FOR RAPID STIMULATION OF INTERACTING
FRACTURES**

by

Cheng Cheng

B. S. in Geology and Geophysics, University of Missouri, Rolla, 2013

M. S. in Petroleum Engineering, University of Pittsburgh, 2015

Submitted to the Graduate Faculty of
Swanson School of Engineering in partial fulfillment
of the requirements for the degree of
Master of Science

University of Pittsburgh

2015

UNIVERSITY OF PITTSBURGH

SWANSON SCHOOL OF ENGINEERING

This thesis was presented

by

Cheng Cheng

It was defended on

March 25, 2015

and approved by

Robert M. Enick, Ph. D., Professor, Department of Chemical and Petroleum Engineering

Badie I. Morsi, Ph. D., Professor, Department of Chemical and Petroleum Engineering

Andrew P. Bunger, Ph. D., Assistant Professor, Department of Chemical and Petroleum

Engineering

Thesis Advisor: Andrew P. Bunger, Ph. D., Assistant Professor

Copyright © by Cheng Cheng

2015

ENERGY-BASED APPROACH FOR RAPID STIMULATION OF INTERACTING FRACTURES

Cheng Cheng, M.S.

University of Pittsburgh, 2015

Currently, every oil and gas industry operator's motivation is aimed toward attaining optimized, low-cost horizontal well completions. The goal is typically to generate uniform, simultaneously-growing hydraulic fractures from 3-6 initiation/entry sites that are spaced within a certain interval of the wellbore comprising a so-called "stage". Due to the stress interaction among growing hydraulic fractures, however, it is hard to stimulate all hydraulic fractures to grow simultaneously in the array. This phenomenon, referred to as a stress shadow, inhibits the growth of inner fractures and favors the growth of outer fractures in the array. Recently, we created a new hydraulic fracture simulator, C2Frac, which very rapidly simulates the growth of an array of hydraulic fractures. The simulation helps reduce the negative effects of stress shadow by determining an optimal perforation spacing. In this model, the fractures created from all perforation clusters were restricted to radial, planar growth. This coupled mathematical model uses the power estimate, asymptotic solutions, and local integration to develop a relationship between the fluid flow entering the well bore and friction pressure drop that approximately accounts for the stress interaction between fractures. Utilizing this relationship, C2Frac can determine how the radius, width, pressure, and total fracture area evolve with time and compare them with a fully coupled benchmark model. The solution is found to be sufficiently accurate for practical purposes and C2Frac completes the calculation in less than 2 seconds compared with the benchmark model that took approximately 1 week to solve the same problem.

Perforation loss, that is, the pressure drop of fluid through the perforation tunnel on the casing, is another important but sometimes neglected effect on fracture growth. So we add the perforation loss into C2Frac to simulate how perforation loss influence the total fracture surface area obtained from a growing array of hydraulic fractures that are impacted by the stress shadow effect. Our results show the potential of proper perforation diameter and number to double the fracture surface area generated by a given injected fluid volume though minimizing the negative

effect of interaction. This approach is known as “limited entry design”. The investigation concludes with devising limited entry design and optimal spacing for different numbers of entry points.

In summary, C2Frac is shown to provide useful approximation to the growth of arrays of hydraulic fractures under the influence of stress shadow and limited entry. By using a novel energetic approach to account for the coupling among the hydraulic fractures and through judicious use of asymptotic, approximate solutions, C2Frac computes in 10^{-6} - 10^{-5} of the computation time required by the most efficient existing model that fully solves the coupled problem. This enables completion optimization because over a thousand trial cases can be run in a single hour of computation in order to search for the best completion configuration, whereas existing models would require tens of years of processor time to perform the same task.

TABLE OF CONTENTS

TABLE OF CONTENTS.....	vi
LIST OF FIGURES	viii
ACKNOWLEDGEMENT	x
1.0 INTRODUCTION	1
2.0 MODEL	4
2.1 PROBLEM STATEMENT AND SIMPLIFICATION ASSUMPTION.....	4
2.2 SOLUTION METHOD	8
2.3 COMPUTING THE POWER TERMS.....	15
2.3.1 Elastic Strain Energy.....	15
2.3.2 Work of Interaction.....	16
2.3.3 Fluid Dissipation.....	19
2.4 ALGORITHM.....	21
3.0 BENCHMARKING.....	23
4.0 EXAMPLE OF OPTIMIZING FRACTURE SPACING	29
5.0 LIMITED ENTRY.....	32
5.1 UNIFORM PERFORATION CLUSTER DESIGN	34
5.2 NON-UNIFORM PERFORATION CLUSTER DESIGN	39
5.3 EXAMPLE OF OPTIMAL FRACTURE DESIGNS	43

5.3.1	Optimal perforation location and limited entry design for five fractures.	
	43	
5.3.2	Limited entry design for six fractures.....	46
6.0	CONCLUSION.....	50
	BIBLIOGRAPHY.....	53

LIST OF FIGURES

Figure 1. A penny-shaped hydraulic fracture, it shows a cross-section through a circular hydraulic fracture with far field case $R \ll h$.	5
Figure 2. Geometric configuration of a hydraulic fracturing stage of length Z with an array of N hydraulic fractures in which h_k is the fracture spacing. The arrows show the interaction stress between fractures.	7
Figure 3. σ_I is the interaction stress which focuses in the radial area which is related to the nearest-neighbor fracture. The yellow area is the corresponding interaction acting area of fracture i on fracture j .	17
Figure 4. The interaction term used in the algorithm.	21
Figure 5. Flow chart of algorithm for 5 fractures	22
Figure 6. C2Frac Compare with ILSA in uniform array that a) $h_1=5m$ and non-uniform array that b) $h_1=4m$ and c) $h_1=3.6m$.	25
Figure 7. C2Frac compare with ILSA on Total fractured area $A_{total}(t, h_1)$. For uniform case a) $h_1=5m$, non-uniform case b) $h_1=4m$ and c) $h_1=3.6m$.	27
Figure 8. Total fracture area ratio $A(T, h_1)/A(T, h_1 = 5m)$ vary with h_1 for pumping time $t = 50s$.	30
Figure 9. Total fracture area ratio $A(T, h_1, h_2)/A(T, h_1 = 4m, h_2 = 4m)$ vary with h_1 and h_2 for pumping time $t = 25s$	31
Figure 10. Total fractured Area Change with different perforation diameter Dp at 25s.	35
Figure 11. The number of perforations of each cluster n keep same in the increase.	36
Figure 12. Uniform perforation diameter effect on total fracture area for uniform spacing.	36
Figure 13. Optimized fracture spacing change with different perforation diameter Dp and n at a) 5s, b) 25s, c) 50s.	39

Figure 14. Plot total fracture area evolution with h_I at 25s with $n=5$. a) $Dp(\text{outer})=0.006$ m is held constant while varying the perforation diameter for the inner and middle fractures. b) $Dp(\text{inner})$ and $Dp(\text{middle})$ are held constant (0.006 m) while varying the perforation diameter for the outer fracture.	40
Figure 15. Plot total fracture area evolution with h_I at 25s for the optimized Dp described before. a), $n(\text{outer})$ is constant. b), $n(\text{inner})$ and $n(\text{middle})$ is constant.	42
Figure 16. Total fracture area evolve with h_I at different treat time. a) without perforation loss, b) the optimal perforation design.	44
Figure 17. The Total fracture area as a function of treat time for non-optimized and optimized design respectively.	45
Figure 18. $A(t, h_1, h_2)$ vary with different Dp for constant n at uniform spacing.	46
Figure 19. $A(t, h_1, h_2)$ vary with different n for constant Dp at uniform spacing.	47
Figure 20. Area of optimized entry design compare with non-optimized at the uniform spacing.	48
Figure 21. Radius of optimized entry design compare with non-optimized at the uniform spacing.	48
Figure 22. Area of optimized entry design compare with ideal design at the uniform spacing. ..	49

ACKNOWLEDGEMENT

This research is under the advisement of A.P. Bunger. The support is gratefully acknowledged. The author would like to thank A.P. Peirce for providing the results of the numerical simulations with ILSA. Also thanks to N. Zolfaghari; his general assistance to the Matlab coding is also deeply appreciated.

1.0 INTRODUCTION

Hydraulic fracturing (HF) has become a vital technique in the oil and gas industry. Hydraulically pressurized liquid creates fractures in a rock which permits an increased flow of hydrocarbons from the reservoir formation towards the well [2]. Essentially all horizontal wells in unconventional reservoirs are stimulated today by hydraulic fracturing in a sequential manner from the “toe” to the “heel” of the well [12]. Although such a multistage (with multiple clusters of perforation comprising the reservoir entry point within each stage) technique has enabled tremendous cost savings, analysis of production logs over several basins tends to show that between 20 to 30 percent of perforation clusters might not contribute to production [16]. One influential factor is the non-uniformity of reservoir properties, including the in-situ stresses, along the well e.g. [3, 6]. Another factor contributing to this loss is the well-known phenomenon known of “stress shadowing.” Stress shadowing refers to suppression of some hydraulic fractures as a result of the compressive stresses exerted on them by nearby hydraulic fractures e.g. [1, 9, 15]. In detail, a stress shadow effect occurs on the fracture surface when spacing between entry points, typically perforation clusters, is small relative to the final fracture length. To more clearly represent the effect, consider one stage that includes three fractures. In this case, growth of the outer two fractures in the array would typically dominate while the growth of the interior fracture would be severely obstructed due to the elevated compressive stresses to which it is subjected relative to the outer fractures. To improve effectiveness of hydraulic fracturing by overcoming

this phenomenon, we need to find a way to simulate how the stress shadow influences the growth of fractures.

Recently, a model built by Peirce and Detournay called ILSA was extended for parallel-planar HF model with full 3D elastic coupling between the simultaneously propagating fractures by Peirce and Bungler [17]. The ILSA model tracks the growth of hydraulic fractures through the transition from a radial storage model to a PKN storage model. It demonstrates that the stress shadow effect can be reduced with appropriate placement of interior HFs close to the outer HFs to inhibit their growth relative to the other fractures in the array [17].

Although ILSA is a benchmark in this research area, the model requires a week or more to compute a single result. Our new model, the C2Frac model, requires only seconds. It achieves this rapid computation time through a novel approximation to the fully-coupled problem. The main innovation is coupling together the influence of the stress shadow through the impact on the overall energy balance of the system. By further approximating the stress interactions through asymptotic expansions of known, analytical elastic crack solutions, the computations avoid full elastic field calculations. Through further approximation using asymptotic solutions for penny-shaped fluid-driven fracture in an impermeable rock by Savitski and Detournay [20], the model eventually determines the crack aperture $W_i(t)$, the net pressure $P_i(t)$, the fracture radius $R_i(t)$, and flow rate $Q_i(t)$ as a function of the fracture number i and pump time t for different values of spacing h . These results will contribute to determining the perforation spacing that hydraulic fracturing can achieve the most fracture area for a certain pumping time.

Additionally, we consider perforation loss in the C2Frac model. The perforation refers to a hole punched in the casing or liner of an oil well to connect it to the reservoir. n perforations distributed in one perforation cluster over a length of about 2 to 5 ft (0.6 to 1.5 m) depending on perforating gun size [12]. Perforation loss uses the analysis of the pressure drop as fluid flows

through a cluster of n perforations (Crump and Conway 1988, Economides and Nolte 2000) based on the power estimate principle. We found that perforation pressure drop can be utilized to counteract the stress shadow effect same as [13].

The thesis is organized as follows: in chapter 2, we introduce the model; in chapter 3, though numerical experiment, we make illustrative graph for uniform array and other non-uniform array to indicate how perforation spacing effects the fracturing and compare the results with ILSA; in chapter 4, we utilize C2Frac model to search for the optimized perforation location to provide an example that C2Frac is a promising model to develop for different research goal; in chapter 5, though C2Frac we make limited entry design; Finally in chapter 6, we make an conclusion and talk about some future work need to do.

2.0 MODEL

C2Frac is an approximate simulator with the capability of carrying out an entire coupled simulation in less than 2 seconds on a desktop computer. This section provides a brief description of the problem to be solved as well as a description of the assumptions and simplifications that underlie the C2Frac algorithm.

2.1 PROBLEM STATEMENT AND SIMPLIFICATION ASSUMPTION

For a typical hydraulic fracturing (HF) treatment of an oil or gas well, the fracture is created by injecting a viscous fluid from the well bore. The fracture is placed within a rock formation that contains the hydrocarbons (the reservoir), and propagates perpendicularly to the minimum in situ confining stress σ_{min} (see Figure 1). The hydraulic fractures are considered to grow transversely toward the horizontal well. As illustrated by Figure 2, this problem examines the growth of N fractures within a single stage and, for now, neglects the stresses induced by the previous stage, noting that these previous-stage stress interactions can be accounted for with a straightforward extension of the approach. An array of N planar fractures distributed within one stage of length Z

is depicted in Figure 2. Hence, the spacing $h_{i,i+1}, i-1, \dots, N-1$ between fracture i and fracture $i + 1$ is such that:

$$Z = \sum_{i=1}^{N-1} h_{i,i+1} \quad (1)$$

During the entire period of growth, the fractures are assumed to remain planar and radial as in Figure 1. This idealization neglects deviation of the fracture path which could result from the presence of a height growth barrier, interactions with natural fractures, or stress shadowing from other hydraulic fractures. A height growth barrier, which exists in most reservoirs, causes a transition from radial to blade-like ("PKN" after cites) growth [19, 14]. Based on similar arguments to those described in detail by Ref [5,17],

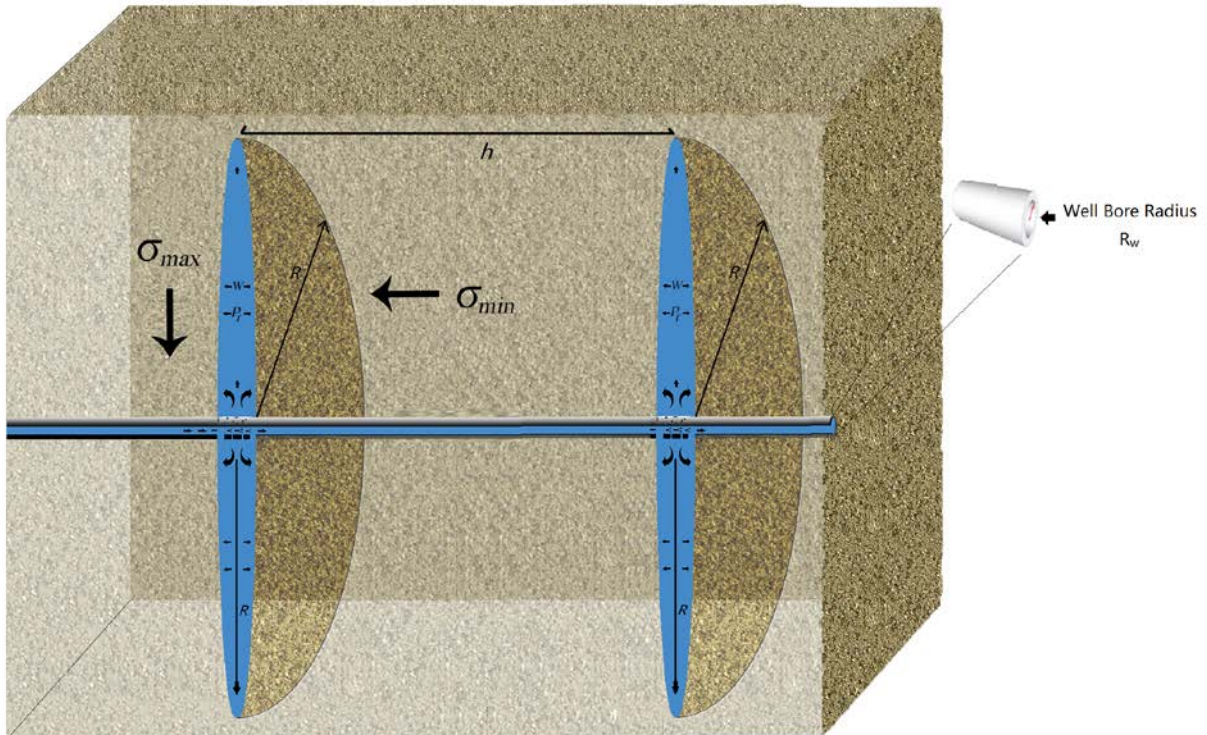


Figure 1. A penny-shaped hydraulic fracture, it shows a cross-section through a circular hydraulic fracture with far field case $R \ll h$.

As long as the impact of the curving on the energy required to drive the hydraulic fractures represent only a small correction to the leading order term(s), the model should remain valid for gently curving hydraulic fractures. Although additional efforts are being directed toward capturing the transition to PKN-like growth, the principle of the modeling method provides a valid representation of radial growth while the fracture radius is less than 70% of the limited fracture height. Unfortunately, the presence of natural fractures cause an unknown impact on the energetics of hydraulic fracturing. Until a further understanding of this relationship is obtained, the interaction with natural fractures will remain unclear.

The radially-growing, planar hydraulic fractures are therefore considered to be driven by an incompressible Newtonian fluid through a homogeneous, impermeable, brittle elastic rock. The fluid is thus characterized by its dynamic viscosity (letting $\mu' = 12\mu$). The rock is characterized by $K' = K_{IC}\sqrt{32/\pi}$ for fracture toughness, K_{IC} , and $E' = E/(1-\nu^2)$ for Young's modulus, E , and Poisson's ratio, ν . Note that accounting for fluid leakoff to the rock, heterogeneity of in situ stress, other reservoir mechanical properties, and/or modeling other fluid rheology is a relatively straightforward as an extension to the present work that is nonetheless beyond the present scope.

The fluid injected, at a total volumetric rate $Q(t)$, is partitioned dynamically to the N perforation clusters. Here we initially neglect the near-wellbore pressure losses due to fracture tortuosity and/or perforation friction as well as pressure losses associated with fluid flow through the inside of the casing between the perforation clusters. The impact of pressure loss through the perforations will be added to the model in Chapter 5. Throughout this analysis, fluid is

considered to be injected from a wellbore of radius R_w at the center of each of the radially-growing hydraulic fractures (Figure 2).

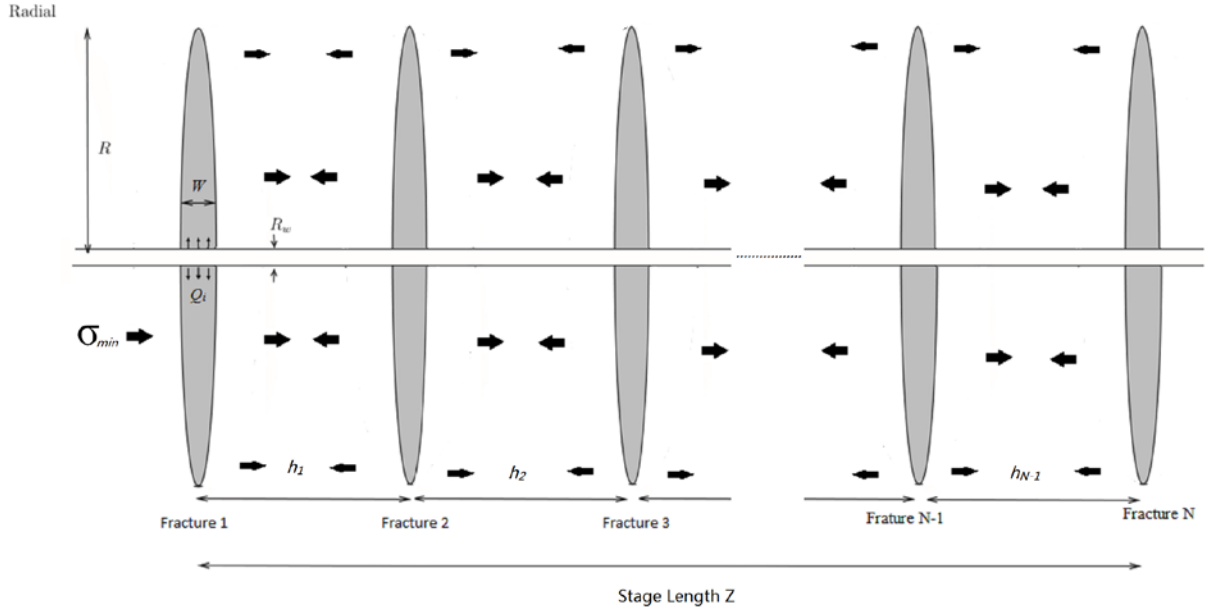


Figure 2. Geometric configuration of a hydraulic fracturing stage of length Z with an array of N hydraulic fractures in which h_k is the fracture spacing. The arrows show the interaction stress between fractures.

For the array of N hydraulic fractures, there are $5N$ unknowns. They consist of, for each fracture indexed i with i going from 1 to N (Figure 2), the opening $w_i(r, t)$, fluid net pressure $p_i(r, t)$ (taking $p_i = p_f - \sigma_{min}$ for fluid pressure p_f), fracture radius $R_i(t)$, elastic interaction stress from the other fractures $\sigma_i(r, t)$, and inlet flow rate $Q_i(t)$. The problem involves finding these $5N$ unknowns as a function of given quantities $Q, \mu', K', E', R_w, N, h_{i,i+1}$, and t .

2.2 SOLUTION METHOD

The problem described has been previously solved using the fully-coupled, multi-planar hydraulic fracture simulator ILSA II ([17], noting that ILSA II is the multi-fracture version of ILSA, [18]). As discussed in the introduction, our goal here is to make the roughest approximation that provides useful results and can be obtained from a very rapidly-computing model. We will therefore use ILSA II as our benchmark and utilize the same underlying governing equations as those upon which ILSA II is built.

Recall the $5N$ unknown quantities: fracture opening $w_i(r, t)$, fluid pressure $p_i(r, t)$, radius $R_i(t)$, elastic interaction stress from the other fractures $\sigma_i(r, t)$, and inlet flow rate $Q_i(t)$. Therefore, five unknowns require $5N$ equations (and appropriate boundary conditions) for the problem to be solved. Following classical hydraulic fracture models [11, 14, 19], $3N$ equations are provided by the coupled system of partial-integro-differential equations from Reynolds lubrication equation for laminar fluid flow, elastic coupling between pressure and opening for a fracture of a certain radius, and propagation according to linear elastic fracture mechanics [19]. An additional N equation is obtained from the interaction stresses which occur when multiple hydraulic fractures grow in close proximity to one another. The stresses are accounted for based on the solution for the stress field around an elastic crack being exposed to an arbitrary internal pressure distribution

(e.g. Crouch and Starfield). The system is closed by the $N-1$ equations given by the constraint that the pressure is the same at every entry point (because they are tied by the wellbore) along with the 1 equation from the constraint that the sum of fluid injected to all entry points must equal the total injection rate $Q(t)$, that is:

$$P_1(0,t)=P_2(0,t)=\dots=P_N(0,t) \quad (2)$$

$$Q(t) = \sum_{i=1}^N Q_i(t) \quad (3)$$

In the benchmark simulations from ILSA II, these coupled equations are solved in a fully-coupled manner using an Implicit Level Set Algorithm - hence ILSA [18]- that accounts for the full 3D elastic interactions among all of the fractures subject to the constraints from equations (2) and (3) (Peirce and Bungler In Press). In the limiting case of a single hydraulic fracture driven by constant-rate injection and that is propagating in either the limit of zero fluid viscosity or zero toughness, ILSA precisely converges to the semi-analytical solutions for a radial hydraulic fracture given by [1]. This convergence of the full model to an asymptotic solution in the limit of non-interacting hydraulic fractures gives a leading order approximation

$$w_i(r,t) \rightarrow \hat{w}_i(r,t) \quad (4)$$

$$R_i(t) \rightarrow \hat{R}_i(t) \quad (5)$$

$$p_i(r,t) \rightarrow \hat{p}_i(r,t) \quad (6)$$

where the hatted quantities correspond to the solution of a radial hydraulic fracture from Savitski and Detournay (2002). While it is possible to consider the zero viscosity limit, for the demonstration of the method we limit consideration to the zero toughness limit. Only considering the zero toughness limit is valid provided that [2]

$$\left(\frac{E^{13} \mu^5 Q_0^3}{K^{18} t^2} \right)^{1/5} \gg 1, i=1, \dots, N$$

In this limit the hatted quantities are given by [1]

$$\hat{w}_i(r, t) = W\Omega(\rho), \quad W = \left(\frac{\mu^2 \langle Q_i \rangle^3 t}{E^2} \right)^{1/9} \quad (7)$$

$$\hat{R}_i(t) = \gamma L, \quad L = \left(\frac{E \langle Q_i \rangle^3 t^4}{\mu} \right)^{1/9} \quad (8)$$

$$\hat{P}_i(r, t) = \sigma_{\min} + P\Pi(\rho), \quad P = \left(\frac{\mu E^2}{t} \right)^{1/3} \quad (9)$$

where $\rho = r/R$, $\langle Q_i \rangle$ is the mean injection rate given by

$$\langle Q_i \rangle = \frac{\int_0^t Q_i dt}{t} \quad (10)$$

and

$$\begin{aligned} \Omega_{m0}^{(1)} / \gamma_{m0}^{(1)} &= \left[\frac{\sqrt{70}}{3} C_1^{(1)} + \frac{4\sqrt{5}}{9} C_2^{(1)} (13\rho - 6) \right] (1-\rho)^{2/3} \\ &+ B^{(1)} \left[\frac{8}{\pi} (1-\rho)^{1/2} - \frac{8}{\pi} \rho \arccos \rho \right] \end{aligned} \quad (11)$$

$$\Pi_{m0}^{(1)} = A_1^{(1)} \left[\omega_1 - \frac{2}{3(1-\rho)^{1/3}} \right] - B^{(1)} \left(\ln \frac{\rho}{2} + 1 \right) \quad (12)$$

$$\gamma \cong 0.6955 \quad (13)$$

Note that in the time stepping algorithm (see Section 2.4), we use $\gamma = 0.7349$ instead of Eq. (13) when calculating R . This is a modification that has been tuned to obtain a better match to the ILSA benchmark.

The solution of ref. [1], reflected by Eqs. (7-9) and (11-13), is strictly valid when the injection rate is constant. Here we have to allow the rate to be non-constant because of the dynamic partitioning of fluid to each of the N fractures in the array. By using the mean, $\langle Q_i \rangle$ we assure that the approximation is consistent with volume balance even if it is not strictly applied to the situation for which it was derived. A similar approach has been proposed by (cite Garagash)[10]. Also note that the logarithmic singularity in the pressure implied by Eq. (12) as $\rho \rightarrow 0$; it is this singularity that requires us to retain the presence and influence of a small but finite wellbore radius R_w .

The main challenge and focus of the problem is due to interaction and the impact of the interaction on hydraulic fracture growth, including the effect on the partitioning of the fluid embodied by Q_i . To obtain the desired solution, the stress interaction must be resolved. Here, instead of solving the stress interaction completely for the σ_i quantities as in the benchmark model, our considerations are limited to the interaction that can be approximated for the far-field asymptotic expansion of the normal stress exerted on a plane located a distance h from a uniformly-pressurized circular crack of radius R . This relationship is described by (after [2])

$$\sigma_I(\rho, \zeta; \langle Q_i \rangle) = -\frac{E' \langle Q_i \rangle t}{\pi h^3} \times \left[1 - \frac{9}{10 \zeta^2} (5\rho^2 + 2) + O(\zeta^{-4}) \right] \quad (14)$$

where $\zeta = h/R$, By letting $\langle Q_j \rangle$ be the mean injection rate to the j^{th} hydraulic fracture and $\zeta_{ij} = h_{i,j}/R_j$ and $\rho_j = r/R_j$, where R_j is the radius of the j^{th} hydraulic fracture and $h_{i,j}$ is the separation between the j^{th} and the i^{th} hydraulic fracture; we can approximate the interaction stresses exerted on the i^{th} hydraulic fracture as

$$\sigma_i(r, t) \sim \hat{\sigma}_i(r, t), \quad \hat{\sigma}_i(r, t) = \sum_{j=1}^{N \neq i} \sigma_I(\rho_j, \zeta_{i,j}; \langle Q_j \rangle) \quad (15)$$

By making these approximations, the model now has $5N$ equations: Eq. (2) giving $N-1$ equations, Eq. (3) giving an additional N equations, $3N$ equations from the substitution of (7-9)

into (4-6), and N equations from Eq. (15). However, the interaction stresses remain uncoupled from the other $4N$ equations. The proposed solution for this issue, which is the critical component of the C2Frac algorithm, is to replace the estimate of the pressure, Eq. (6), with an updated estimate that obtains its correction via an energy balance equation for each hydraulic fracture of the form derived by [2]. This energy balance is given by

$$Q_i(p_{f_i}(0,t) - \sigma_{\min}) = \dot{U} - \dot{W}_I + D_c + D_f \quad (16)$$

Here the left hand side represents the net input power provided by the pumping system and partitioned to the i^{th} hydraulic fracture according to the partitioning of the influx, Q_i . The basic energy balance requires that the input power to each hydraulic fracture is not only conserved, but also partitioned such that a portion of it increases the elastic strain energy stored in the rock (the \dot{U} term), a portion is required to overcome the negative work being created on each hydraulic fracture by the stress interactions from its neighbors (the \dot{W}_I term), and a portion is dissipated. The dissipated portion contributes either in breaking the rock (the D_c terms) or in viscous fluid flow (the D_f term). Making use of the estimates from Eqs. (4-6) and (15) to compute each of the right hand side terms (details to follow), we obtain an updated estimate of the wellbore pressure as

$$p_{f_i}(0,t) \sim \hat{p}_{f_i}(0,t) \quad \hat{p}_{f_i}(0,t) = \sigma_{\min} + \frac{1}{Q_i} \left(\dot{U} - \dot{W}_I + D_c + D_f \right)_{\hat{w}_i, \hat{r}_i, \hat{p}_i, \hat{\sigma}_i} \quad (17)$$

By making use of this updated wellbore pressure estimate, the algorithm couples the hydraulic fractures together via their stress interactions and the required adjustments for the simultaneous satisfying of the constraints on the wellbore pressure and injection rates, Eqs. (2) and (3). Note that while we have assumed uniform reservoir conditions, accounting for variable stress can be incorporated into equation (17) by replacing σ_{min} with a local value $\sigma_{min,i}$. Additionally, recall that for the present demonstration we limit consideration to the zero toughness regime, which corresponds to $D_c \ll D_f$ such that we can simplify Eq. (17) by taking $D_c \rightarrow 0$.

Two main challenges remain. The first is to approximate the energy rate (power) terms on the right hand side of Eq. (17). These estimates were previously derived by [2] for the case of a uniformly-growing, uniformly-spacingd, infinite array of hydraulic fractures. However, the array under consideration consists of a finite number of hydraulic fractures that are not uniformly spacing and receive varying fluid influxes. Estimating these terms for this considerably more complicated situation is the subject of Section 4. The second challenge is to efficiently step through time while providing a solution for the evolution of all N hydraulic fractures. This time stepping algorithm is the subject of Section 5.

To conclude the description of the basic solution method, it is important to recall the motivation: Find the simplest, most efficiently computing model with the capability to obtain useful results which can be used for optimization of hydraulic fracture stage design, i.e. a reasonably accurate indication of fluid partitioning to each entry point, fracture length, and/or of the overall fracture surface area generate by a given treatment. But it is also important to realize that at the outset it is not obvious that the proposed approximation method will work. Its hypothesis is based on capturing the appropriate asymptotic behavior of the hydraulic fractures

as they begin to interact but before they become very long relative to their spacing. By coupling them together in such a way that hydraulic power and fluid volume are both conserved, enough data is provided to sufficiently predict some salient features of the system. However, the only way to justify the approach is a comparison to the benchmark model which does not make these crude simplifications. This benchmarking, as well as the successes and limitations it portrays are the subject of Section 6.

2.3 COMPUTING THE POWER TERMS

2.3.1 Elastic Strain Energy.

Bunger [2] has shown that for a radial hydraulic fracture the rate of change of elastic strain energy is given by

$$\dot{U} = \pi \int_{R_w}^R \left(p \frac{\partial w}{\partial t} + w \frac{\partial p}{\partial t} \right) r dr \quad (18)$$

By the substitution of Eqs. (4-6) with Eqs. (7-9) into Eq. (18), in addition to letting $R_w / R \rightarrow 0$, and solving the integral we obtain,

$$\dot{U} = -0.06215 \left(\frac{E'^2 \langle Q_i \rangle^3 \mu'}{t} \right)^{1/3} \quad (19)$$

2.3.2 Work of Interaction.

Following [2], the rate of work due to interaction from neighboring hydraulic fractures is given by

$$\dot{W}_I = -2\pi \int_{R_w}^R \sigma_I \frac{\partial w}{\partial t} r dr \quad (20)$$

Note that we drop a factor of 2 relative to [2] because we wish to account for the contributions from each neighboring fracture individually, whereas an infinite uniform array is assumed in [2]. Instead of W_I representing the energy required to overcome the rate of work performed on fracture i by the others fractures; we consider W_I as the energy that fracture i performs on the neighboring fractures. From Sneddon (1945), the normal component of stress in the neighborhood of a crack, σ_z , is determined by the location of a point relative to the crack, embodied by scaled coordinates ζ and ρ . Here ζ is the ratio of spacing h to the crack radius R , and ρ is the ratio of radial position r to fracture radius R . The ζ decrease as the fracture grows, that is, as R increases for each fracture. As this happens, the interaction stress becomes more focused in the region near the center of the fracture, $\rho \ll 1$. For the fractures which grow slower than the neighboring fractures, the surface integral in Eq. (20) is therefore approximated in the region of the smaller of the two fracture radii in the interacting pair, as shown in Figure 3.

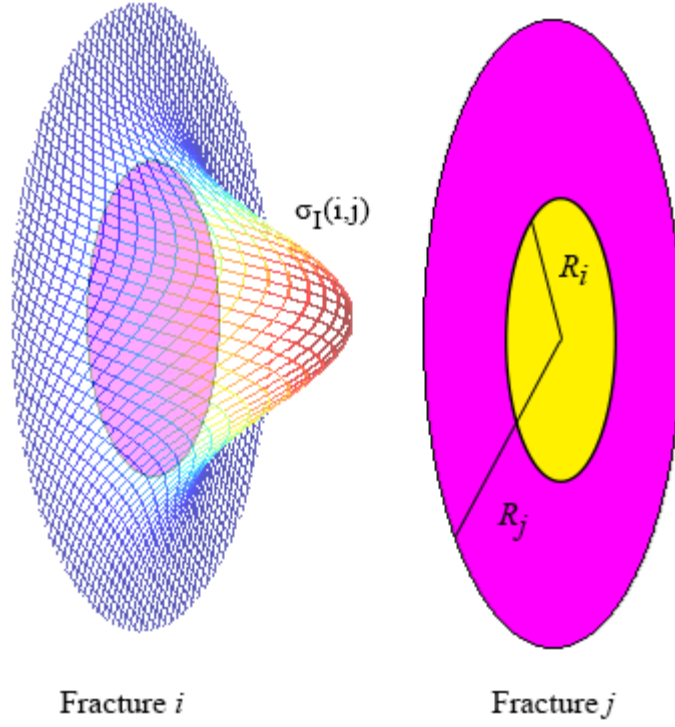


Figure 3. σ_I is the interaction stress which focuses in the radial area which is related to the nearest-neighbor fracture. The yellow area is the corresponding interaction acting area of fracture i on fracture j .

The work of the interaction stress is thus approximated by substitution of equations (4-6) with equations (7-9) along with the interaction stress estimator from Eq. (15).

$$\dot{W}_I \sim E' \langle Q_i \rangle t \sum_{j=1}^{N, j \neq i} \left[-2\gamma^2 \int_{R_w}^{\min(\hat{R}_j, \hat{R}_i)} \frac{t}{w_j} \frac{\partial W_j \Omega}{\partial t} r dr \right] \frac{\hat{w}_j \min(\hat{R}_j^2, \hat{R}_i^2)}{h_{i,j}^3} \quad (21)$$

Substituting Eq. (11) into Eq. (21), the numerical factor of the leading order for fracture i is expressed as

$$\frac{4}{9}\gamma^3 \int_{R_w}^{\min(\hat{R}_j, \hat{R}_i)} \left\{ \begin{array}{l} \left[\frac{\sqrt{70}}{3} C_1^{(1)} + \frac{4\sqrt{5}}{9} C_2^{(1)} \left(13 \frac{x}{\hat{R}_j} - 6 \right) \right] \left(1 - \frac{x}{\hat{R}_j} \right)^{2/3} + \dots \\ B^{(1)} \left[\frac{8}{\pi} \left(1 - \frac{x}{\hat{R}_j} \right)^{1/2} - \frac{8}{\pi} \frac{x}{\hat{R}_j} \arccos \frac{x}{\hat{R}_j} \right] \end{array} \right\} r dr, \quad j \neq i \quad (22)$$

The numerical factor of interaction which depends on the radius ratio of neighboring fractures, is not a constant for the suppressed fractures. However, computing it at each time step would result in 1-2 orders of magnitude increase in computational time. Hence, we assume the numerical factor to be a constant 0.06893 which integral from the simplification $R_i=R_j$. From the numerical experiment result, it is good enough to approximate the ILSA benchmark (Chapter 4). The complete form of interaction power is therefore given by:

$$\dot{W}_i \sim 0.03420E' \langle Q_i \rangle t \sum_{j=1}^{N, j \neq i} \frac{\hat{w}_j \min(\hat{R}_j^2, \hat{R}_i^2)}{h_{i,j}^3}, \quad R_i \ll h_{j,i}, \quad i=1, \dots, N, \quad j \neq i \quad (23)$$

For clarity, we show only the leading order term in the series expansion for $R \ll h$ embodied by Eq. (14). In practice, we found that keeping the next term in the expansion further improved the results relative to the ILSA benchmark.

2.3.3 Fluid Dissipation.

Following [2], the fluid flow dissipation is given by

$$\dot{D}_f = \frac{\pi}{\mu'} \int_{R_w}^R w^3 \left(\frac{\partial p}{\partial r} + \frac{\partial \sigma_t}{\partial t} \right)^2 r dr \quad (24)$$

where, again following [2], this quantity can be split into 3 contributions so that

$$\dot{D}_f = \dot{D}_{f,ln} + \dot{D}_{f,p} + \dot{D}_{f,\sigma} \quad (25)$$

The first of these terms represents the dissipation associated with the logarithmic singularity in the fluid pressure in the limit $R_w \rightarrow 0$, hence it is in this term that our small but finite R_w appears in order to mitigate an infinite dissipation term. The second term is associated with the fluid pressure gradient and the third term is a correction to the fluid pressure gradient due to the interaction stress.

Once again, substituting Eqs (4-6) with Eqs (7-9) and obtaining numerical coefficients by evaluating the integrals, the leading order expressions for $\dot{D}_{f,ln}$, $\dot{D}_{f,p}$ and $\dot{D}_{f,\sigma}$ are given by

$$\dot{D}_{f,ln} \sim -0.04637 \left(\frac{E'^2 \langle Q_i \rangle^3 \mu'}{t} \right)^{1/3} \ln \left(\frac{R_w^9 \mu'}{E' \langle Q_i \rangle^3 t^4} \right)^{1/9} \quad (26)$$

$$\dot{D}_{f,p} \sim 0.2136 \left(\frac{E'^2 \langle Q_i \rangle^3 \mu'}{t} \right)^{1/3} \quad (27)$$

$$\dot{D}_{f,\sigma} \sim 0.4319 \left(\frac{E'^{11} \langle Q_i \rangle^9 t^{17}}{t} \right)^{1/9} \sum_{j=1}^{N, j \neq i} \frac{\hat{w}_j^3 \min(\hat{R}_j^2, \hat{R}_i^2)}{h_{j,i}^5} \quad (28)$$

Note that the numerical factor of $\dot{D}_{f,\sigma}$ is obtained from the integral

$$36\gamma^2 \int_{R_w}^{\min(\hat{R}_i, \hat{R}_j)} \Omega_j^3 \left| \frac{\partial \Pi_i}{\partial \left(\frac{r}{R_i} \right)} \right| r^2 dr \quad (29)$$

which is simplified here as a constant 0.4319 by assuming $R_i=R_j$.

The interaction term, Eq (28), is extended to account for the higher order terms in the stress approximation, Eq. (14). We determined that including the next order correction, as shown in Eq. (14), requires numerical parameters of $\dot{D}_{f,ln}$ to be 0.2 to moderately improved the agreement with the benchmark solution.

2.4 ALGORITHM

In C2Frac model, quantities are assumed to be equal for every cluster at the start time t_I , which corresponds to 0.01 second. In each time loop, the model will calculate Q_i , then W_i , R_i and P_i will be calculated by Eq.(7),(8) and (9) to return values into governing equations for next loop computing. The simulation is allowed to proceed until the predetermined treatment time is reached, with the duration of each time step selected such that further refinement does not result in a change in the solution of more than a couple percent.

$\textcircled{1} \dot{W}_I \sim \frac{E' \langle Q_{outer} \rangle^t}{h_{inner,outer}^3} (\hat{w}_{inner} \hat{R}_{outer}^2)$	$\textcircled{5} \dot{W}_I \sim \frac{E' \langle Q_{inner} \rangle^t}{h_{inner,middle}^3} (\hat{w}_{middle} \hat{R}_{inner}^2)$
$\textcircled{2} \dot{W}_I \sim \frac{E' \langle Q_{outer} \rangle^t}{h_{inner,outer}^3} (\hat{w}_{inner} \hat{R}_{inner}^2)$	$\textcircled{6} \dot{W}_I \sim \frac{E' \langle Q_{inner} \rangle^t}{h_{inner,middle}^3} (\hat{w}_{middle} \hat{R}_{middle}^2)$
$\textcircled{3} \dot{W}_I \sim \frac{E' \langle Q_{inner} \rangle^t}{h_{outer,inner}^3} (\hat{w}_{outer} \hat{R}_{inner}^2)$	$\textcircled{7} \dot{W}_I \sim \frac{E' \langle Q_{middle} \rangle^t}{h_{middle,inner}^3} (\hat{w}_{inner} \hat{R}_{inner}^2)$
$\textcircled{4} \dot{W}_I \sim \frac{E' \langle Q_{inner} \rangle^t}{h_{outer,inner}^3} (\hat{w}_{outer} \hat{R}_{outer}^2)$	$\textcircled{8} \dot{W}_I \sim \frac{E' \langle Q_{middle} \rangle^t}{h_{middle,inner}^3} (\hat{w}_{inner} \hat{R}_{middle}^2)$

Figure 4. The interaction term used in the algorithm

The main challenge in the algorithm is to deal with various combinations of shorter and longer neighboring fractures interacting with one another. An example is given here for the case of 5 fractures. Figure 4 shows the specification of Eq. (23) to various combinations of larger and

smaller inner, outer, and middle fractures. The selection of the interaction term approximation is illustrated by the flow chart in Figure 5, which refers to the approximations in Figure 4 by number.

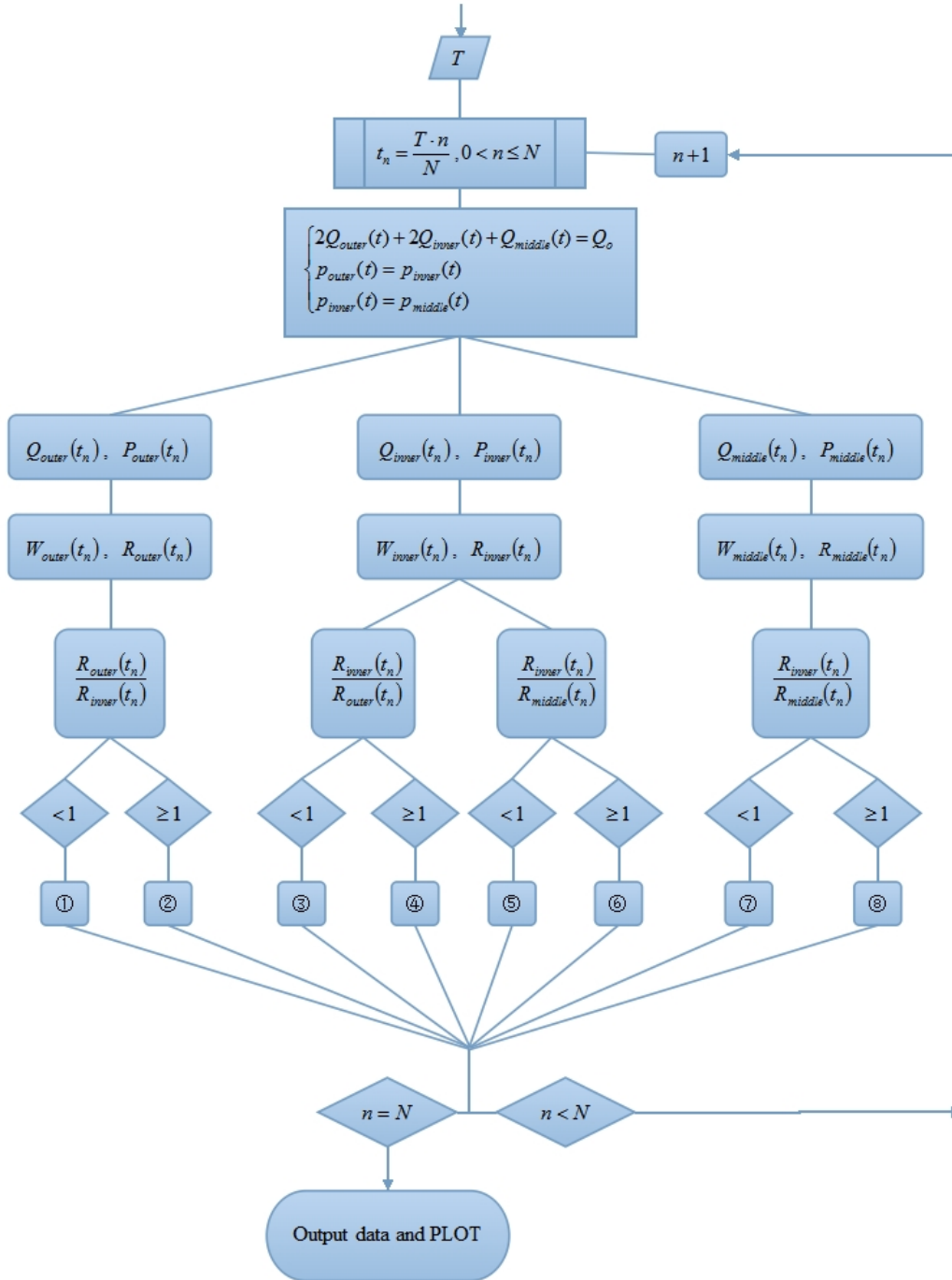


Figure 5. Flow chart of algorithm for 5 fractures

3.0 BENCHMARKING

The numerical results are mainly impacted by the number of fractures, the perforation locations, and by the relative importance of energy dissipation associated with rock breakage versus viscous fluid flow. Benchmarking will first be demonstrated considering cases with $N=5$. To be consistent with the far field expression for the elastic interaction stress, we limit consideration to growth up to the point where the ratio $R(t)/Z$ becomes 0.5 for the longest fracture in the array, where Z is the total span of the fracture array (i.e. stage length, see Figure 2). In these benchmarking cases, the fractures are located symmetrically with respect to the middle fracture, i.e. fracture 1 is identical to fracture 5 and fracture 2 is identical to fracture 4. In order to make a reliable comparison with the benchmark ILSA model, identical parameters were utilized in the simulations for each model beginning with the following parameter set:

$$E=9.5 \text{ GPa}, \nu=0.2, K_{IC}=0 \text{ MPa}\cdot\text{m}^{1/2},$$

$$\mu=1 \text{ Pa}\cdot\text{s}, Q_o=0.1 \text{ m}^3/\text{s}, Z=20 \text{ m},$$

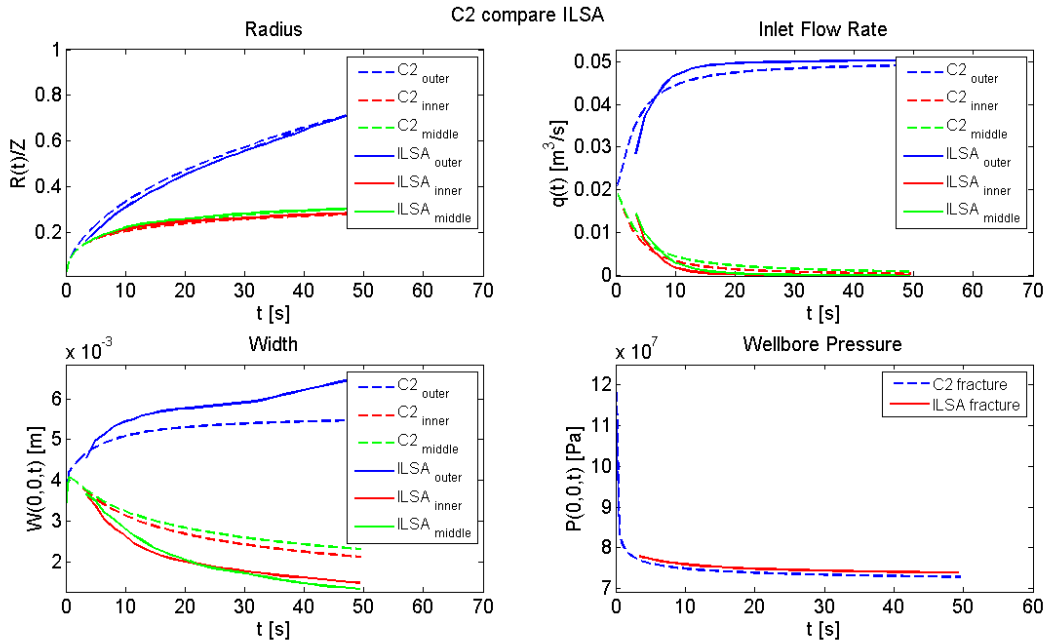
$$\sigma_{zz}^0=70 \text{ Mpa}, R_w=0.2\text{m}.$$

recalling that parameters E and ν represent Young's modulus and Poisson's ratio, respectively, while K_{IC} is the fracture toughness, μ is the dynamic viscosity of the fracturing fluid, Q_o is the total influx of fluid supplied to the well-bore, and Z is the stage length (see Figure 2). The well-

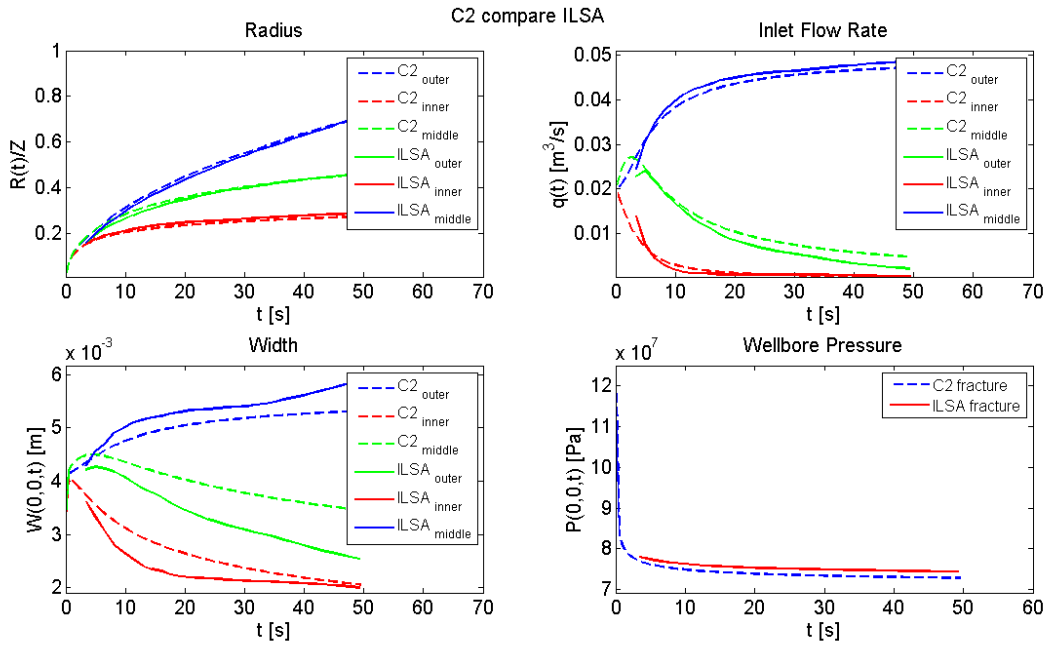
bore is assumed to be straddled by the ambient geological confinement field σ_{zz}^0 caused by the overlying layers. For further clarification, fracture 1 and 5 are named outer fractures; fracture 2 and 4 are named inner fracture; fracture 3 is named middle fracture.

Figure 6 depicts how fracture length, width, fluid flux, and well bore pressure change with time for uniform and non-uniform perforation spacing. Figure 6(a) corresponds to uniform spacing such that $h_I = 5$ m and the stage length $Z = 20$ m. The fracture planes thus have z-axis coordinates $z_1=0, z_2=5, z_3=10, z_4=15, \text{ and } z_5=20$. Figure 6(b) introduces a modification to the uniform array in which fractures 2 and 4 are moved such that $h_I=4$. The corresponding fracture planes have z coordinates $z_1=0, z_2=3.5, z_3=10, z_4=16.5, \text{ and } z_5=20$. Figure 6(c) depicts a similar non-uniform case in which $h_I=3.6$ m. The corresponding fracture planes have z coordinates $z_1=0, z_2=3.6, z_3=10, z_4=16.4, \text{ and } z_5=20$.

(a)



(b)



(c)

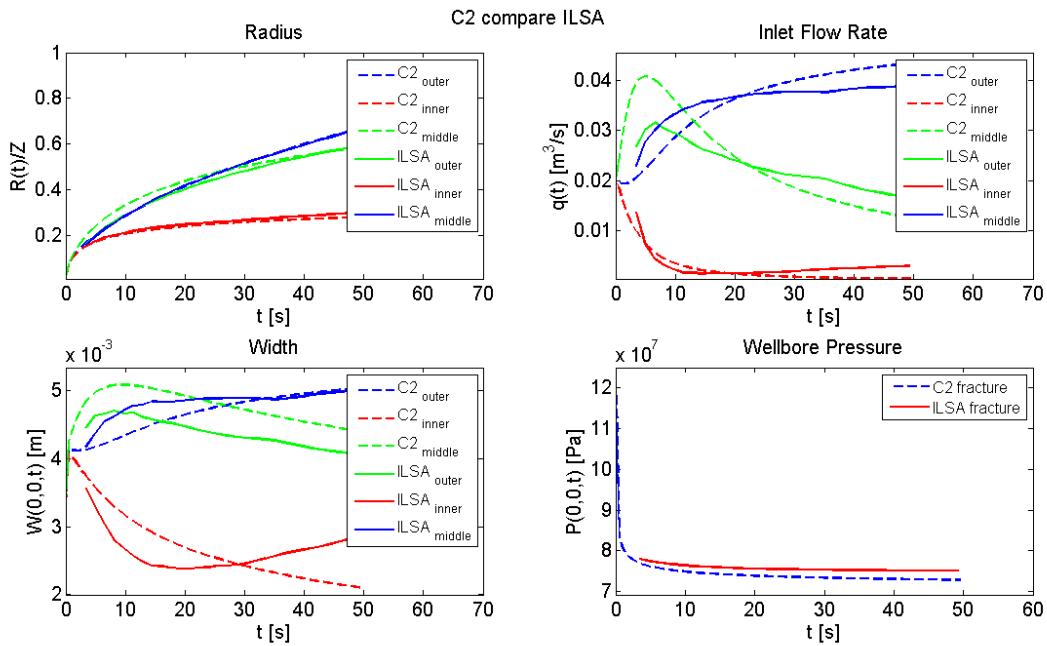


Figure 6. C2Frac Compare with ILSA in uniform array that a) $h_I=5m$ and non-uniform array that b) $h_I=4m$ and c) $h_I=3.6m$.

Focusing firstly on the case of uniform spacing, Figure 6a shows that similar to ILSA, the outer fractures of the C2Frac model grew preferentially while other fractures were suppressed. After 20 seconds, the influx of outer fracture inlet increases sharply to $0.05 \text{ m}^3/\text{s}$ and consumes nearly all the injection flow. On the contrary, flow rate of other fractures decrease to approach zero. Upon changing the spacing h_1 from 5m to 3.6m, the inlet rate of outer fractures decreases from 0.05 (Figure 6a) to 0.045 (Figure 6c). This decrease in injection rate to the outer fractures is accompanied by an increase to the middle fracture, which increases from 0.005 in the uniform spacing case (Figure 6a) to 0.01 in Figure 6(c). In all 3 cases the flow rate to inner fracture remains almost unchanged. A detailed discussion of the behavior of 5 fracture arrays with various non-uniform spacings is provided by Peirce and Bungler [5].

Most importantly, since the purpose is to benchmark C2Frac to ILSA, the length prediction for all fractures agrees within a few percent. The predicted wellbore pressure also agrees within a few percent in all cases. Meanwhile, the fluid influx to each fracture is within about 10-20% of the benchmark. The worst match is in the fracture opening at the wellbore, which is in about 10% discrepancy for the outer fracture and as much as 50% for the inner and middle fractures. Nonetheless, for practical purposes the estimates are very good, especially if the goal is to predict the extent of fracture growth and the fluid pressure that will be generate.

Since the total fractured area is potentially a scaling factor for primary recovery of hydrocarbons from each fracturing stage, agreement with the predictions of total fractured area is important because it can serve as a suitable parameter to maximize as a way of optimizing the effectiveness of a given HF treatment [16]. Here we define $A_{total}(t, h_1)$ which is the summation of $A_i(t, h_1)$ over all the fractures i of the $N=5$ fracture array versus time t for a representative selection of values of the configuration perturbation parameter h_1 . Initially, when all the fractures are small, so that their mutual interactions are insignificant, all configurations generate surface

area at roughly the same rate and almost linearly with the time. However, for $t > 20$ s, because of the ever-increasing interaction effect, the $h_1=3.6$ m case generates more new fracture area (Figure 7c) than the other two cases, depicted in Figure 7(a) and Figure 7(b). On the other hand, to show the similarity between C2Frac and ILSA further, we compare the total fractured area of C2Frac with ILSA. From Figure 7, we realize C2Frac remain 20m^2 more than the ILSA throughout 50s, this constant fractured area difference between C2Frac and ILSA exists due to the initial value given in ILSA at five seconds. Such similarity between C2Frac and ILSA lasts until 50 seconds, which correspond the ratio R_{max}/Z is 0.7 such that the far field approximation of the elastic interaction is expected to no longer be valid.

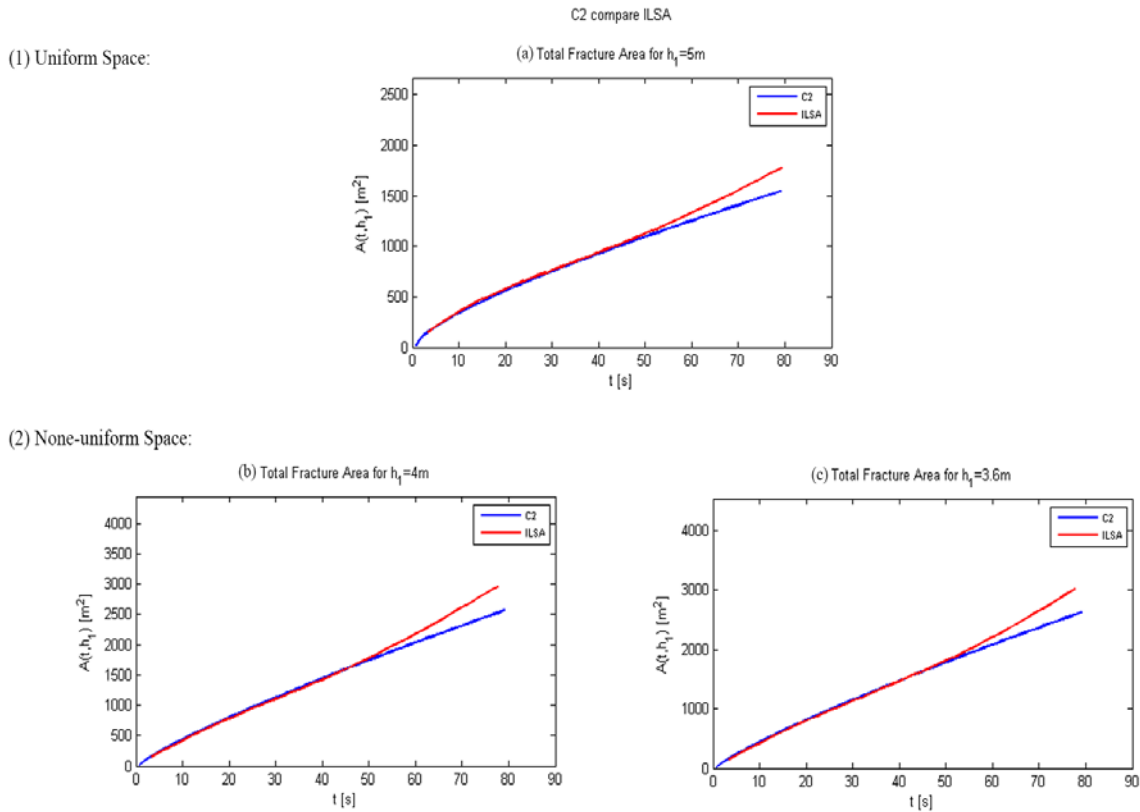


Figure 7. C2Frac compare with ILSA on Total fractured area $A_{total}(t, h_1)$. For uniform case a) $h_1=5\text{m}$, non-uniform case b) $h_1=4\text{m}$ and c) $h_1=3.6\text{m}$.

Combining Figures 6 and Figure 7 we can conclude that C2Frac is divergent from the ILSA model when R_{max}/Z is greater than 0.7. Noted in the assumption, C2Frac model simulates the radial growth only in the far field expression range that $R \ll Z$, but the ILSA model makes use of a full elastic solution for arbitration fracture separation, hence it has no such limit.

In summary, we find that this benchmarking shows the C2Frac approach to be promising, but it is currently limited to the first minute or so of treatments that are normally 50-100 minutes long. Accounting for the larger time behavior will require C2Frac to account both for near-field elastic interaction and for the transition from radial to blade-shaped geometry. These extensions will be considered in future work.

4.0 EXAMPLE OF OPTIMIZING FRACTURE SPACING

We have seen that for $t < 50$ s, C2Frac approaches the ILSA on the uniform and non-uniform case. As a result, we consider the total fractured area $A(T, h_I)$ in the array up as a function of the configuration parameter h_I until time T which a chosen pump time around 45s (obviously this time would be different for a different set of input parameters such as injection rate, fluid viscosity, and rock properties). The normalized fracture area, given by $A(T, h_I)/A(T, h_I=5m)$, represents the impact of changing the spacing relative to using uniform spacing. This normalized fracture area is plotted in Figure 8, with h_I varying from 0.1m to 9.9m. We observe that the least total normalized fractured area, 63%, is obtained for $h_I = 0.3$ m, that is, when the inner fractures are placed extremely close to the outer fractures.

When h_I becomes smaller than 0.3m, the middle fracture occupies most of the inflow from well bore while the outer and inner fractures are suppressed greatly, approximating the case of a single fracture. Interestingly, in this limit of a single fracture the created surface area is large. However, it is reasonable to assume that the total oil or gas recovery of one stage will decrease in the long term because of limiting production to the vicinity of a single fracture; that is, the stimulation reservoir volume will be much smaller.

The optimal spacing is shown to correspond to $h_I = 3.07$ m. This spacing fractures 7% more area than the uniform case. As a measure of the robustness of this optimum, we observe the total fractured area can be increased by more than 44% by selecting the optimized $h_I = 3.07$ m instead

of $h_1=0.3m$. Note also that this result is shown after 50s of fracturing; Peirce and Bungler [5] have shown that increases in the fracture area of more than 50% can be obtained from a model that can be run to larger times.

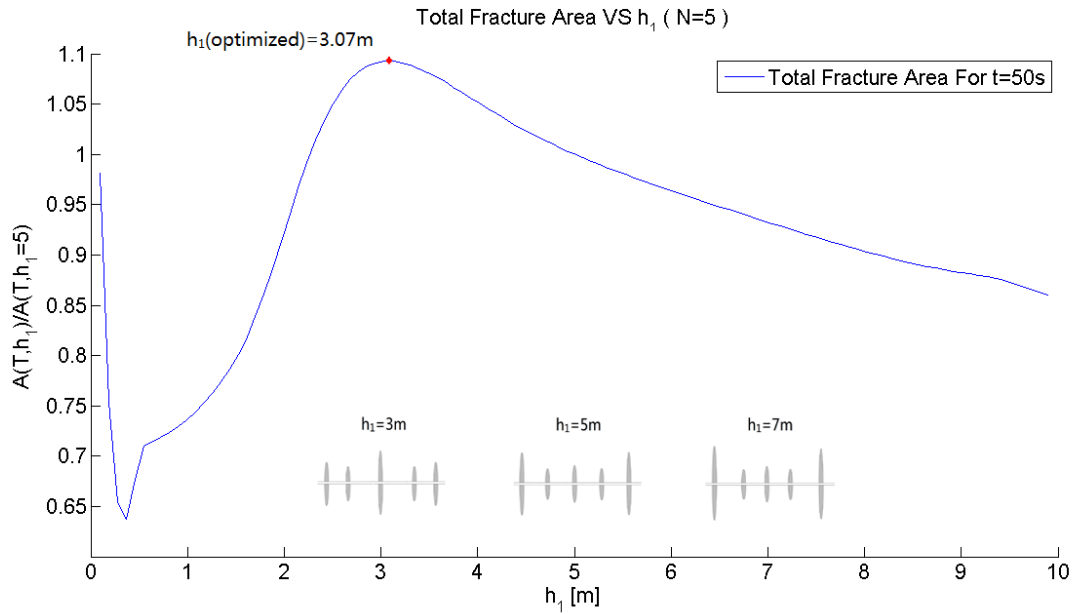


Figure 8. Total fracture area ratio $A(T, h_1)/A(T, h_1 = 5m)$ vary with h_1 for pumping time $t = 50s$.

To further illustrate the use of C2Frac, we modify to consider an array of 6 fractures. A similar benchmarking ILSA to the one presented for 5 fractures in Chapter 3 confirmed the validity of the solution. Hence, we have used C2Frac to perform an optimization of the fracture surface area in terms of 2 spacing parameters, h_1 and h_2 giving the spacing between fractures 1-2 and 2-3, respectively (see Figure 2). The result is shown in Figure 9, where the fracture area is normalized again by the uniform spacing case, that is $A(T, h_1, h_2)$ divided by $A(T, h_1 = 4m, h_1 = 4m)$. The simulations therefore predict an optimum when h_1 is around 2.5m and h_2 is around 4m.

Here the optimum corresponds to about 6% more fracture area than the uniform case and 16% more than the worst situation. Once again, the impact of selecting the optimal spacing is expected to increase with time (cite Peirce and Bungler), but the current version of C2Frac can only be used up to the point that the longest fracture is about 0.6 times the stage length.

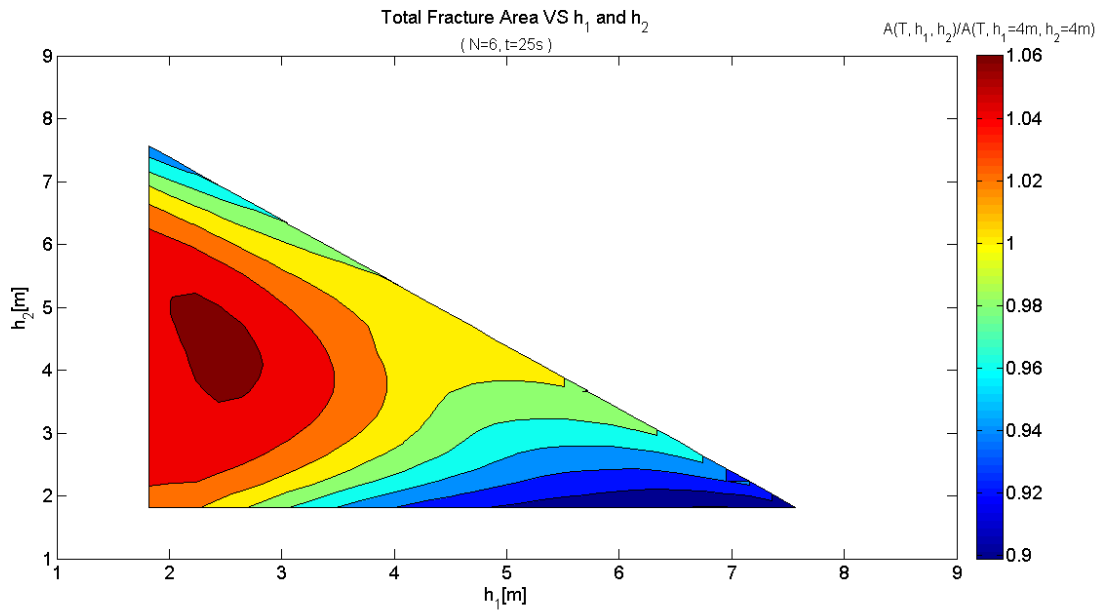


Figure 9. Total fracture area ratio $A(T, h_1, h_2)/A(T, h_1 = 4m, h_2 = 4m)$ vary with h_1 and h_2 for pumping time $t = 25s$

5.0 LIMITED ENTRY

In C2Frac, we vary the spacing between the planes in the array of fractures and measure the stress shadow effect on flow rate, radius, width and pressure. For each such configuration the solutions have been compared with Peirce's ILSA model. The data shows that it provides accurate approximations in the far field expression range by limited treat time. In a further step, we add the perforation loss into the C2Frac as a power contribute. This step makes use of the analysis of the pressure drop as fluid flows through a cluster of n perforation holes (Crump and Conway 1988, Economides and Nolte 2000). The perforation pressure drop is accounted for in C2Frac by adding the rate of energy loss (power loss) through the perforations to the right and side of the energy balance, Eq. (16), and running the algorithm as otherwise unchanged. Using Crump and Conway's solution [7], the power loss is given by [5].

$$P_{perf} = N \left(\frac{a\rho}{n^2 D_p^4 C^2} \right) Q_i(t)^3 \quad (31)$$

The N in Eq. (31) represents the number of perforation clusters in one hydraulic fracturing stage, as previously illustrated in Figure 2. Each cluster has n perforations; usually this value is within the range of 5 to 20, and it ideally should be the number of holes that actually

accommodate the fluid flow into the hydraulic fracture, not just the total number placed (some of which may be plugged or otherwise ineffective). Here also D_p represents the perforation diameter, which is usually within a range from 6 to 15 mm. As before, $Q_i(t)$ represents the injection rate to the i^{th} fracture, which will vary with the treat time t (recall Figure 6). There is also a shape factor for the perforation tunnels themselves, given here by C which is typically taken as 0.56 before erosion(sharp perforation) and 0.89 after erosion based on the experimental results of Crump and Conway (1988). In C2Frac we neglect perforation erosion so C is taken as a constant equal to 0.56. The numerical factor, a , is usually defined as 0.2369. The fluid injected into the reservoir has a fluid density of ρ . Taken together, the bracketed quantities in Eq. (31) comprise a coefficient of proportionality between the power loss associated with flow through the perforations and the square of the flow rate.

Limited entry design refers to manipulation of the pressure loss through each perforation cluster by varying the perforation diameter D_p and/or the number of perforation holes, n [5]. One proposed approach to promoting simultaneous HF growth entails using smaller/fewer holes for the outer fractures and more/larger holes for the inner fractures within an array in order to counteract the stress shadow-driven suppression of the inner fractures (cite Lecampion et al, ARMA 2014).

The limited entry design approach using C2Frac with perforation losses is separated into three steps. First, we design the uniform perforation case with same perforation diameter and number for all clusters. Second, using results from the first step, we design the non-uniform case by changing D_p and n in different clusters to obtain an optimized spacing that is closer to uniform spacing than it would be without the use of limited entry. Third, we compare the optimal and non-optimal designs to determine if fracture spacing optimization combined with limited entry design is worthwhile relative to performing one approach or the other but not both.

5.1 UNIFORM PERFORATION CLUSTER DESIGN

First, we assume that the perforation number n is constant and equal to 12. This assumption corresponds to a middle value in the range of 5 and 20. Next, we run C2Frac to simulate how the total fracture area varies with the perforation diameter. The remaining parameters are defined below:

$$E=9.5 \text{ GPa}, \nu=0.2, K_{IC}=0 \text{ MPa}\cdot\text{m}^{1/2},$$

$$\mu=1 \text{ Pa}\cdot\text{s}, Q_0=0.1 \text{ m}^3/\text{s}, Z=20 \text{ m},$$

$$\sigma_{zz}^0=70 \text{ Mpa}, R_w=0.2\text{m}, \rho=1000\text{g}/\text{cm}^3$$

$$a=0.2369, C=0.56, n=12$$

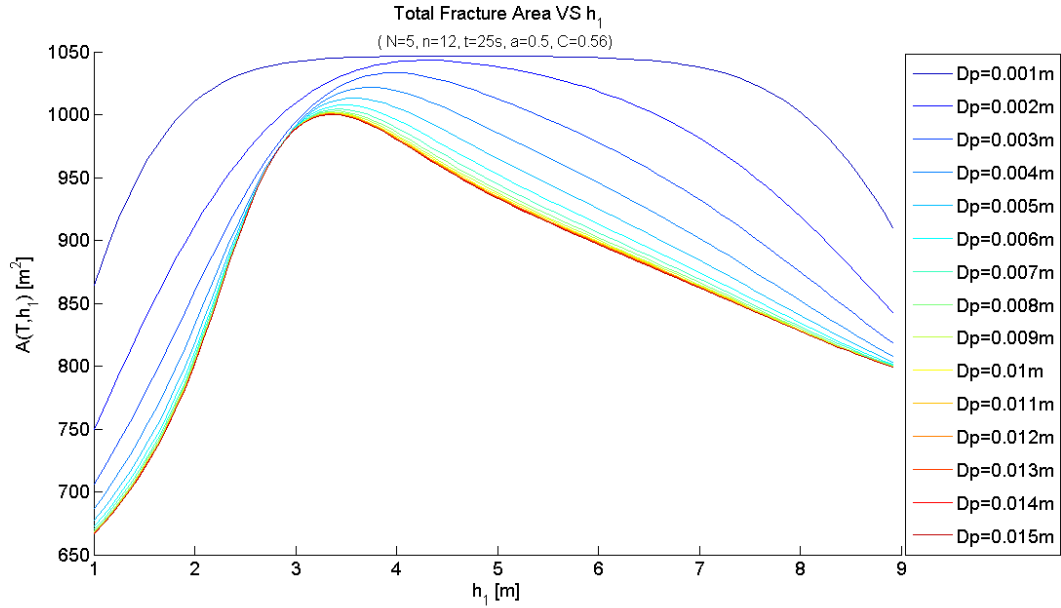


Figure 10. Total fractured Area Change with different perforation diameter D_p at 25s.

From Figure 10, when the perforation diameter is smaller at the same n in every cluster, more fracturing area can be obtained at any perforation spacing. In addition, the maximum point of the curves moves closer to 5m, which is the uniform spacing in this test case. The impact of changing the number of perforations is similar (Figure 11), as expected due to the appearance of both n and D_p in the perforation loss Eq. (31). Similar with Figure 10, less perforations result in more fracturing area and the optimal spacing is more closed to 5m.

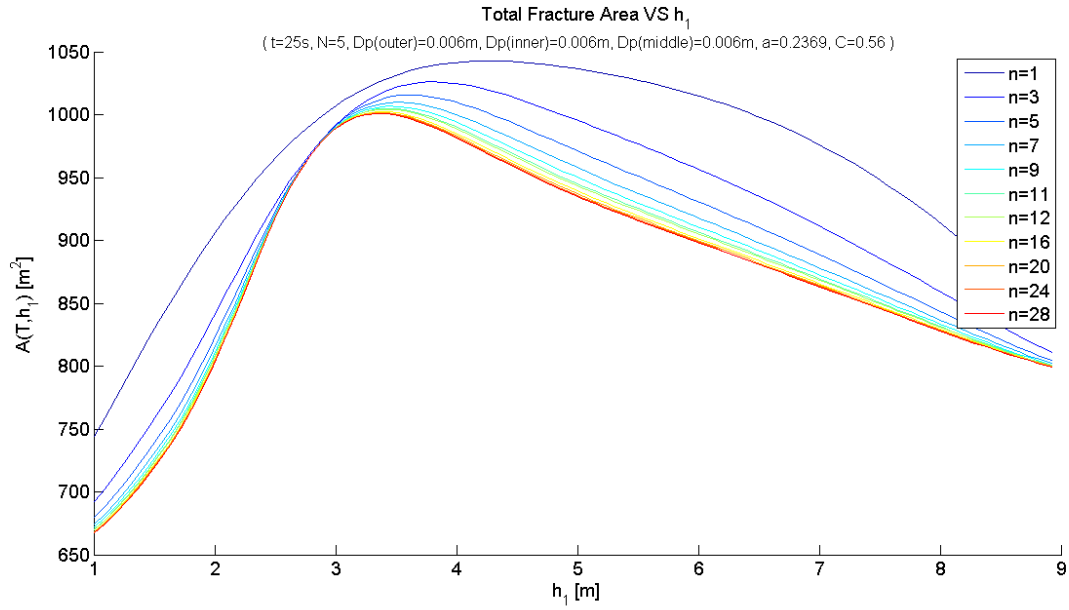


Figure 11. The number of perforations of each cluster n keep same in the increase.

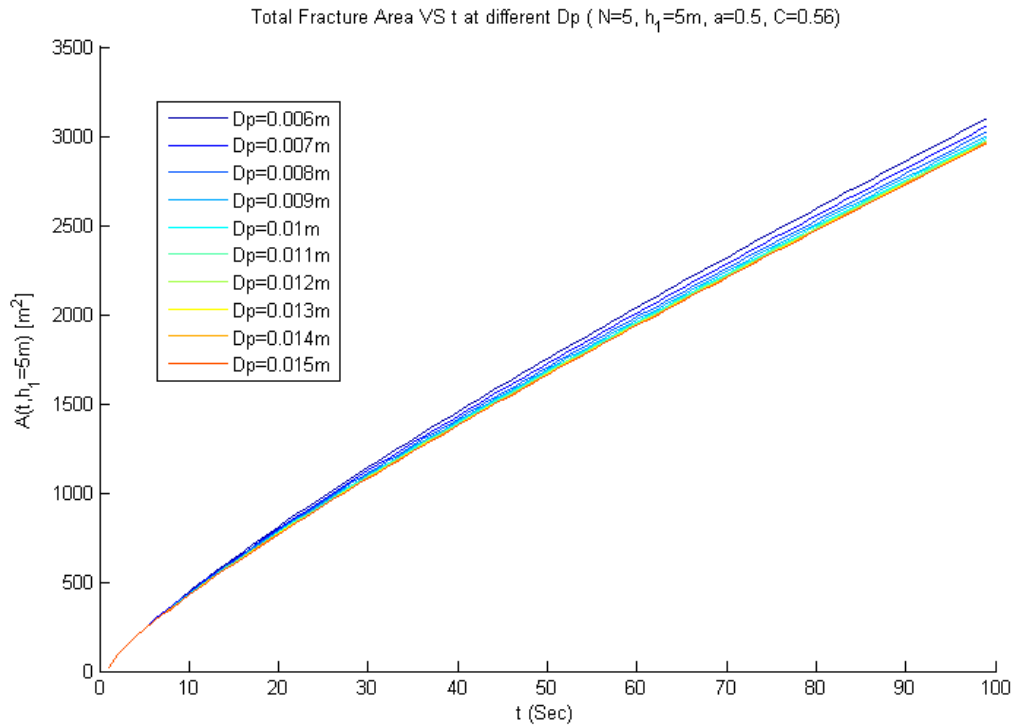
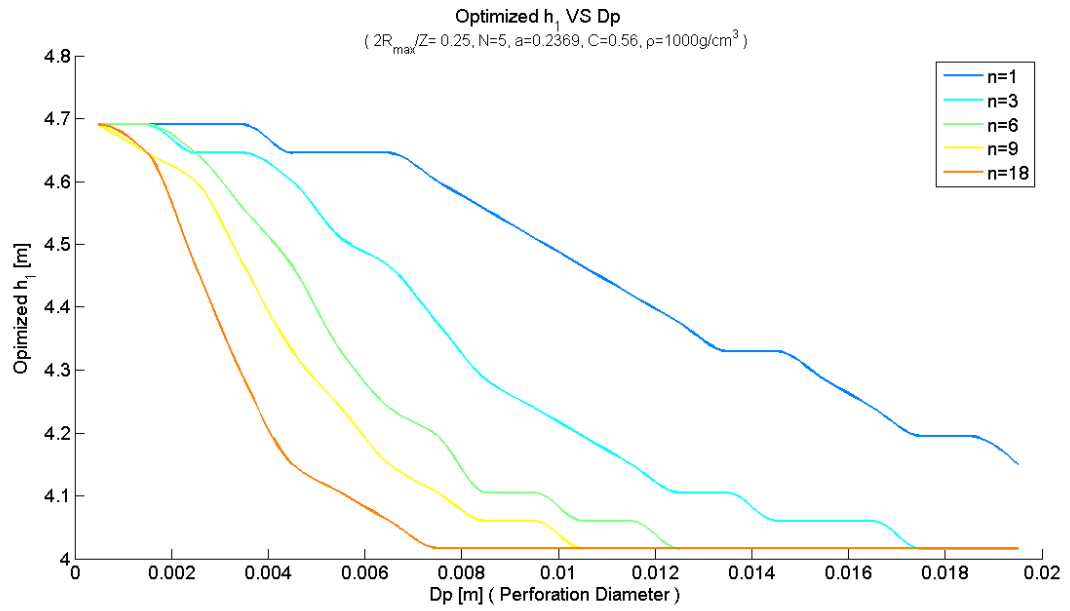


Figure 12. Uniform perforation diameter effect on total fracture area for uniform spacing.

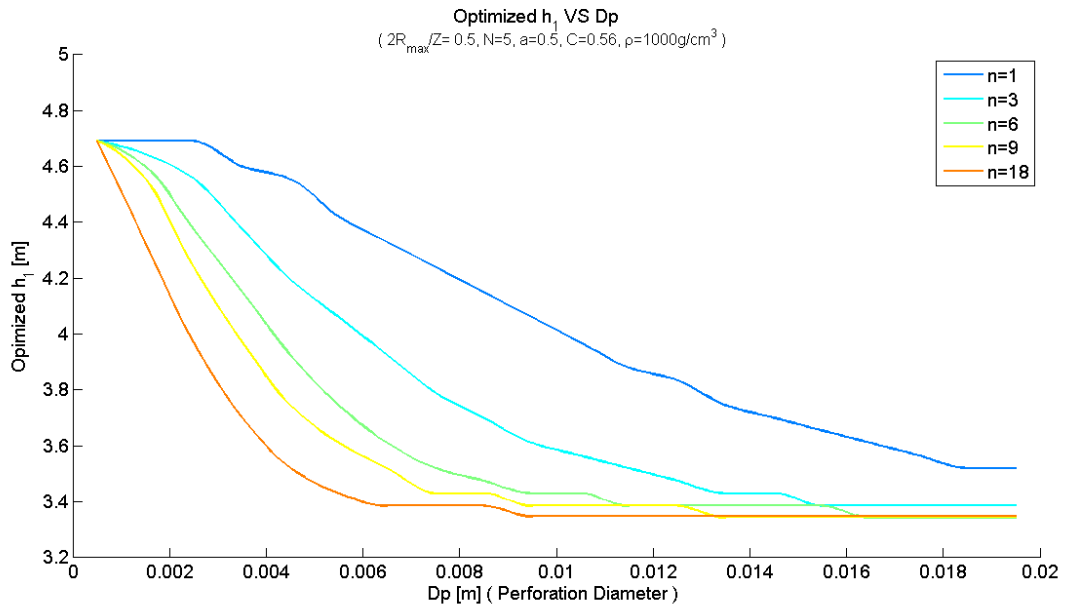
We can also explore the impact of uniform limited entry on the uniform spacing case by selecting the uniform spacing $h_l=5\text{m}$ and varying the perforation diameter varies from 6mm to 15mm, with results shown in Figure 12. Initially, when all the fractures are small, the perforation diameter influence is insignificant. However, as treatment time increases, the smaller perforation diameter case generates more new fracture area because it drives more uniform distribution of fluid among the fractures. At the range of early time that C2Frac can simulate, the impact of decreasing the perforation diameter is around 5-10% .

A practical question arises from these results. If one is given a desired spacing (i.e. h_l), then what is a combination of n and D_p that will generate the greatest fracture surface area. Or, one may similarly ask what is the spacing and number of perforations required to optimize the fracture area for a fixed perforation diameter. This question is addressed in Figure 13. Firstly, it is shown by contrasting Figures 13a-c that the answer depends upon the time of pumping at which the area is to be maximized (this will also be seen in Figure 16). Generally, we can see that utilizing the same perforation diameter and a smaller perforation number results in a larger optimized h_l . Regardless of the perforation number, all the curves converge at small and large diameters – i.e. in the limits of infinite and zero perforation pressure loss.

(a)



(b)



(c)

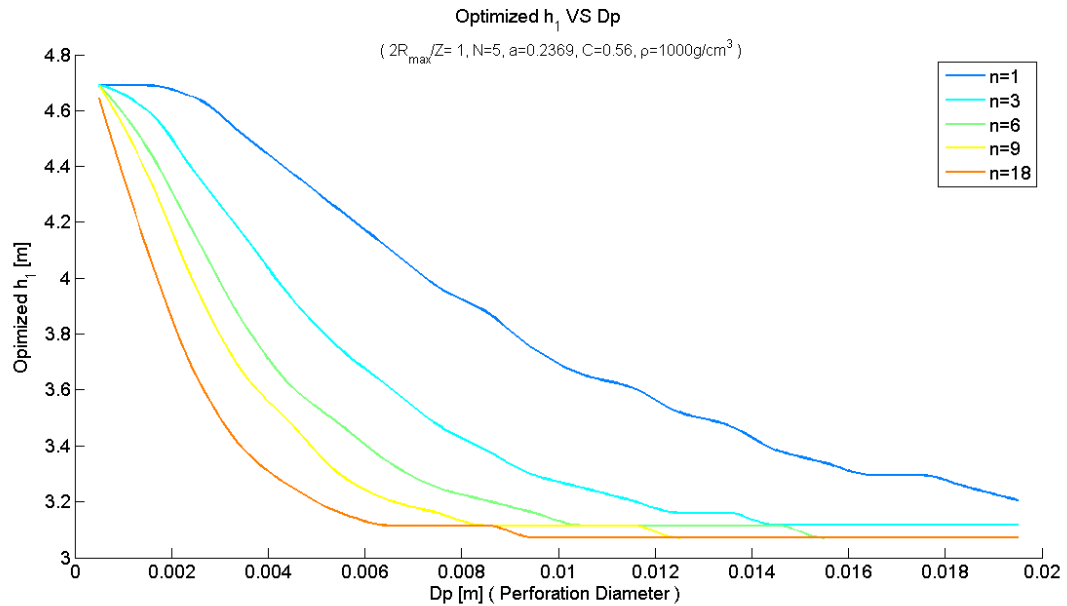


Figure 13. Optimized fracture spacing change with different perforation diameter D_p and n at a) 5s, b) 25s , c) 50s.

5.2 NON-UNIFORM PERFORATION CLUSTER DESIGN

Previously, non-uniform spacing was shown to provide larger fracture surface areas by mitigating the impact of stress shadow. Similarly, we predict that the non-uniform design for perforations should also generate more fracture surface area than the uniform perforation design. C2Frac is used to show the extent to which this hypothesis is true.

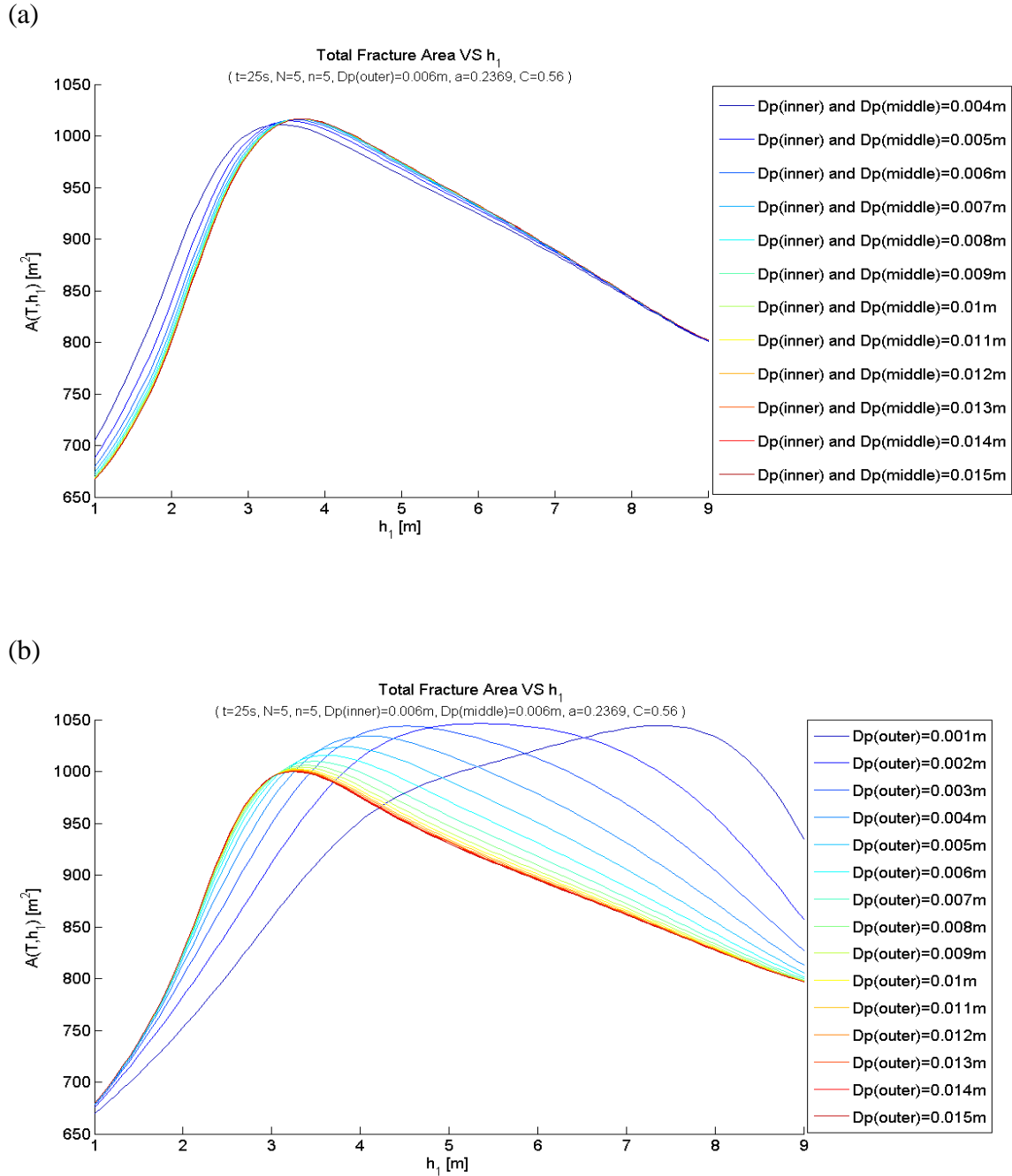
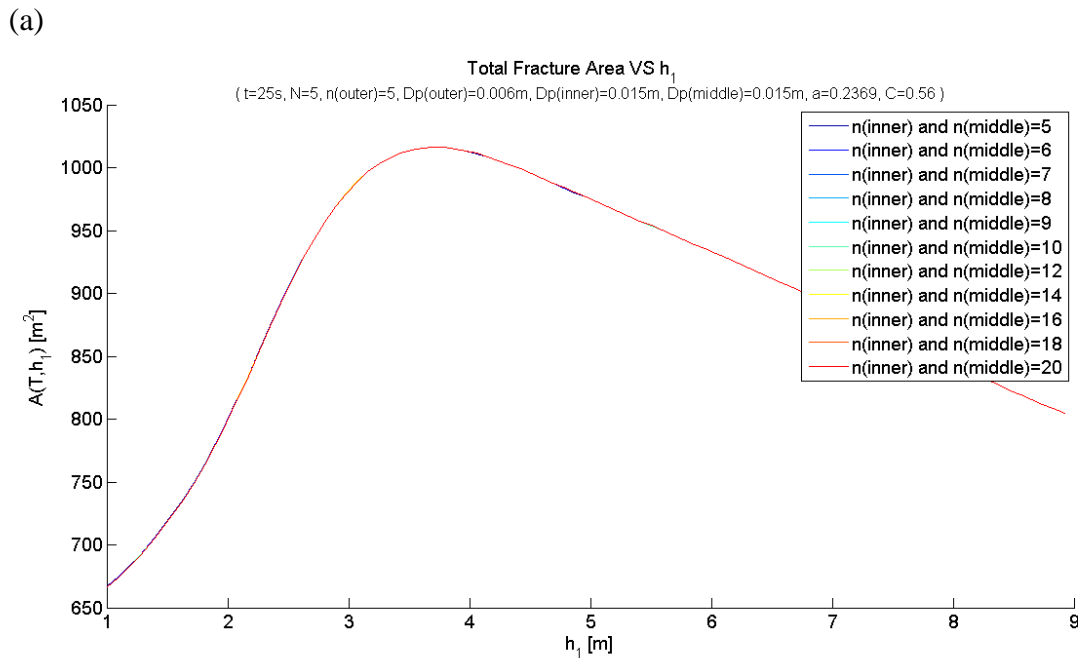


Figure 14. Plot total fracture area evolution with h_1 at 25s with $n=5$. a) $Dp(outer)=0.006$ m is held constant while varying the perforation diameter for the inner and middle fractures. b) $Dp(inner)$ and $Dp(middle)$ are held constant (0.006 m) while varying the perforation diameter for the outer fracture.

To reduce the number of degrees of freedom, perforations in inner and middle clusters are taken to be the same as each other but different from the outer clusters. First we fix $n=5$ and show the variation of the fracture surface area with h_1 and D_p (Figure 14). In Figure 14(a), the perforation diameter of the outer clusters is the same (0.006m) for each case while the inner and middle clusters varied from 0.003 to 0.015m. Figure 14(b) holds the middle and inner diameter at 0.006 m while varying the diameter of the outer fractures from 0.001 to 0.015m. We observe that if the perforation diameter of the outer cluster is smaller in relation to the inner and middle, larger fracture area can be generated with uniformly-spaced clusters. The trend becomes more obvious as the difference in the diameters increases.

Next we choose 0.006m as $D_p(\text{outer})$, 0.015m as $D_p(\text{inner})$ and $D_p(\text{middle})$ and investigate the impact of using different n for different clusters. In Figure 15(a) the n of inner and middle cluster is the variable with n for the outer cluster fixed, while in Figure 15(b) n is fixed for the inner and middle clusters while n for the outer cluster is varied



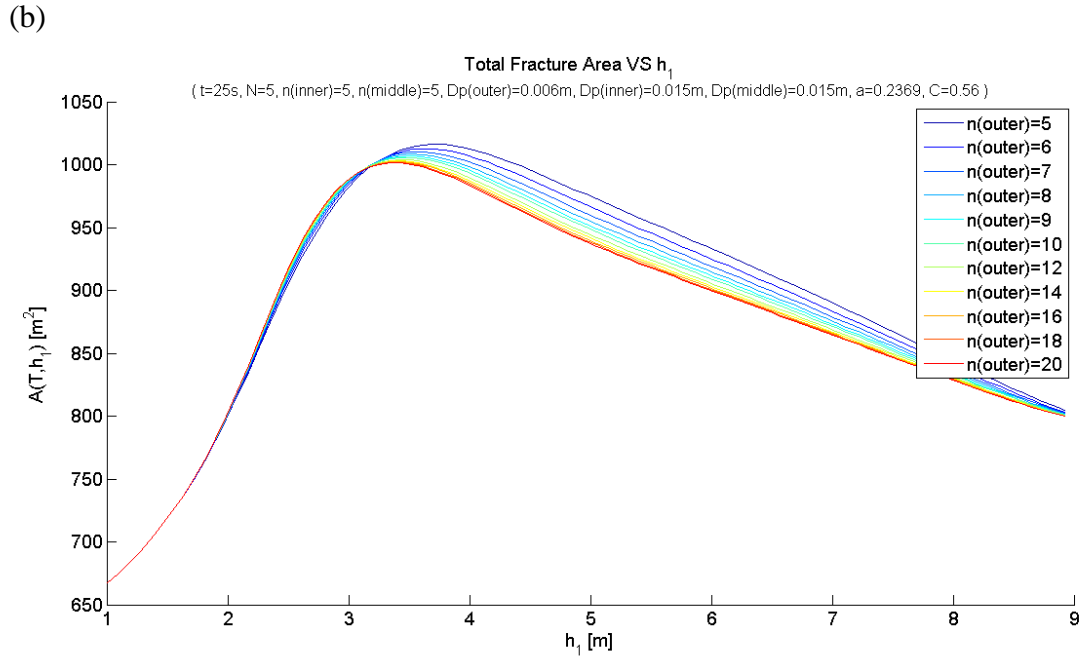


Figure 15. Plot total fracture area evolution with h_1 at 25s for the optimized D_p described before. a), $n(\text{outer})$ is constant. b), $n(\text{inner})$ and $n(\text{middle})$ is constant.

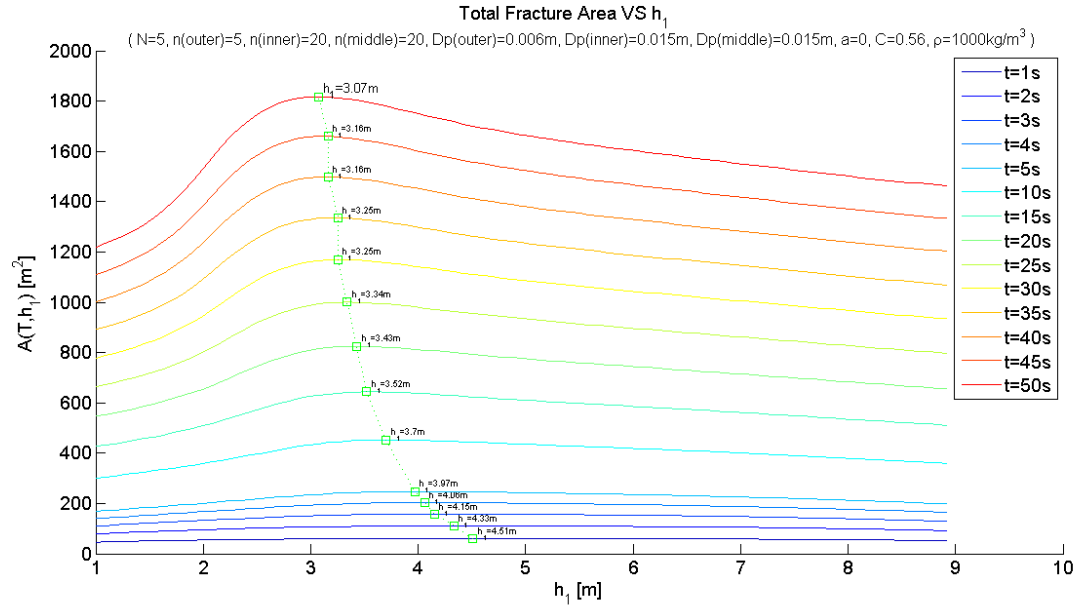
In Figure 15(a) it is hard to distinguish the differences among the cases. A small variation can be seen in Figure 15(b) wherein a smaller value of n for the outer cluster leads to a slightly larger fracture area. The optimal choice for the perforations is $n=5$ for all clusters. But it is clear that varying the perforation diameter has a larger impact than varying the number of perforations. This is not surprising due to the larger power on D_p than n in Eq. (31).

5.3 EXAMPLE OF OPTIMAL FRACTURE DESIGNS

5.3.1 Optimal perforation location and limited entry design for five fractures.

Analysis of the various design cases shows that a uniform spacing design performs better with fewer perforations and with smaller perforation diameter for outer clusters. Using $Dp(\text{outer})=0.006\text{m}$, $Dp(\text{inner})=Dp(\text{middle})=0.015\text{m}$, $n(\text{outer})=5$, $n(\text{inner})=n(\text{middle})=20$, and keeping the other parameters the same as before, Figure 16 plots the total fracture area as a function of h_1 for different treatment times. The first key observation is that as the treatment time is increases, the value of h_1 that gives the greatest fracture area decreases. However, the rate at which it decreases is decreasing with time, suggesting that the optimum h_1 attains some asymptotic value at large time. A second important observation is that the difference in fracture surface area between the optimal case and the uniform spacing case (still $h_1=5\text{m}$) increases with time. There is no reason to suggest this trend would not continue; indeed Peirce and Bungler [5] observe more than 50% difference between optimal and uniform spacing after 140 seconds pumping time for the same input parameters as are considered here but with growth contained to a 20 m high reservoir.

(a)



(b)

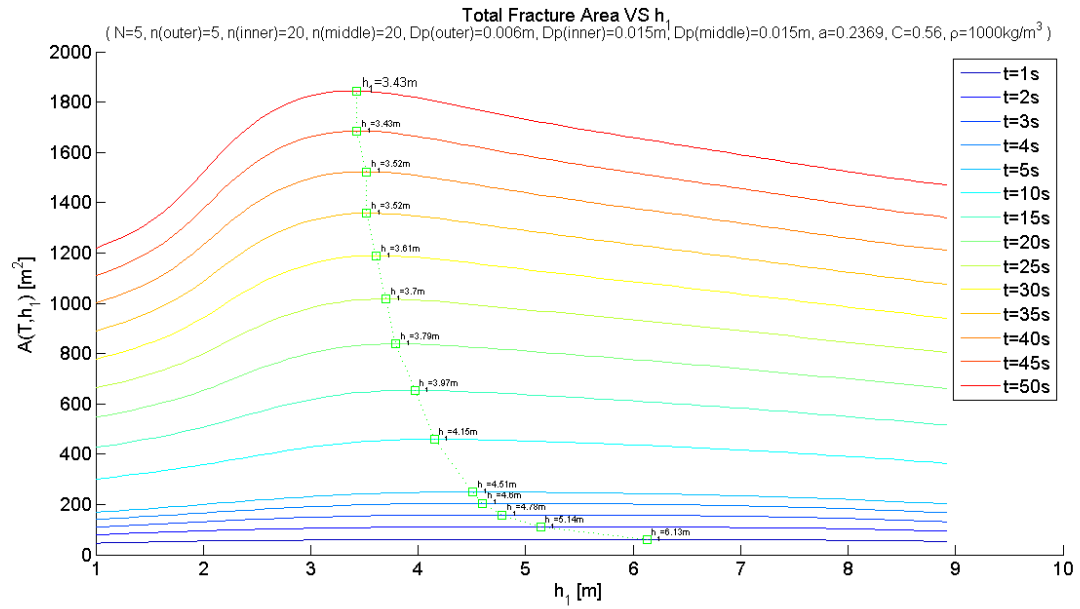


Figure 16. Total fracture area evolve with h_1 at different treat time. a) without perforation loss, b) the optimal perforation design.

In Figure 16(a), the perforation loss is negligible. In general, the perforation-friction entry should be neglected. In Figure 16(b), which gives the result with the optimal limited entry design, the line connecting the maximum points shifts the optimized values of h_1 closer to 5m.

Figure 17 demonstrates the improvement of optimal perforation design. We selected one typical non-optimized design with $Dp=0.015\text{m}$, $n=20$ for all clusters as a comparison objective for our optimal design at the uniform spacing. To combine the optimal perforation location design with limited entry design, we compare two design for the optimal spacing clusters which are denoted in Figure 17 as the purple and red curve. We observe that at treatment time 25 seconds, for uniform spacing, limited entry design creates 50m^3 more fracture area. Such advantages amplify with increasing time. From treat time 25 to 50 seconds, the divergence increase from 50m^3 to 100m^3 or 5% more. When combined with optimal spacing, improvement can approach 15%.

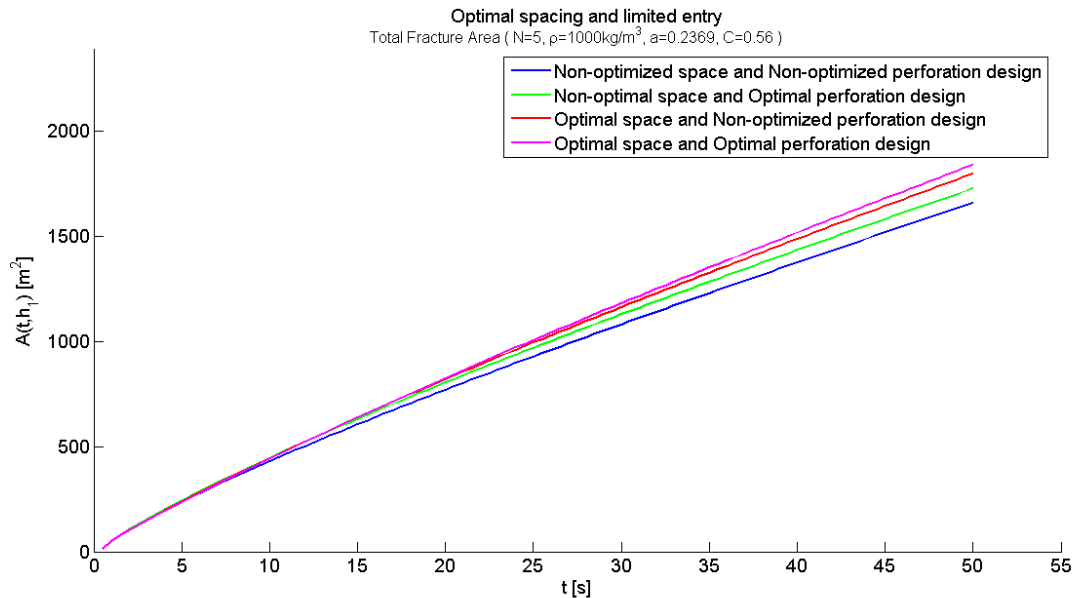


Figure 17. The Total fracture area as a function of treat time for non-optimized and optimized design respectively.

5.3.2 Limited entry design for six fractures.

To further demonstrate the impact of optimized spacing and limited entry design, we extend to six fractures. In order to account for the higher number of variables in the six fracture array, we need to plot 3D figures to show the fracturing efficiency.

In Figure 18, we kept the number of perforations in every cluster as 5, which as previously determined, will produce more fracture area for most spacings. We observe that when $Dp(\text{outer})$ is 0.015m, and $Dp(\text{inner})$ is 0.006m, we get the minimum fracture area 1500m² contrast with 1680m² which focus in the region that Dp_{outer} smaller than Dp_{inner} . In Figure 19, we observe the same phenomenon by the limit that Dp is constant at 0.006m.

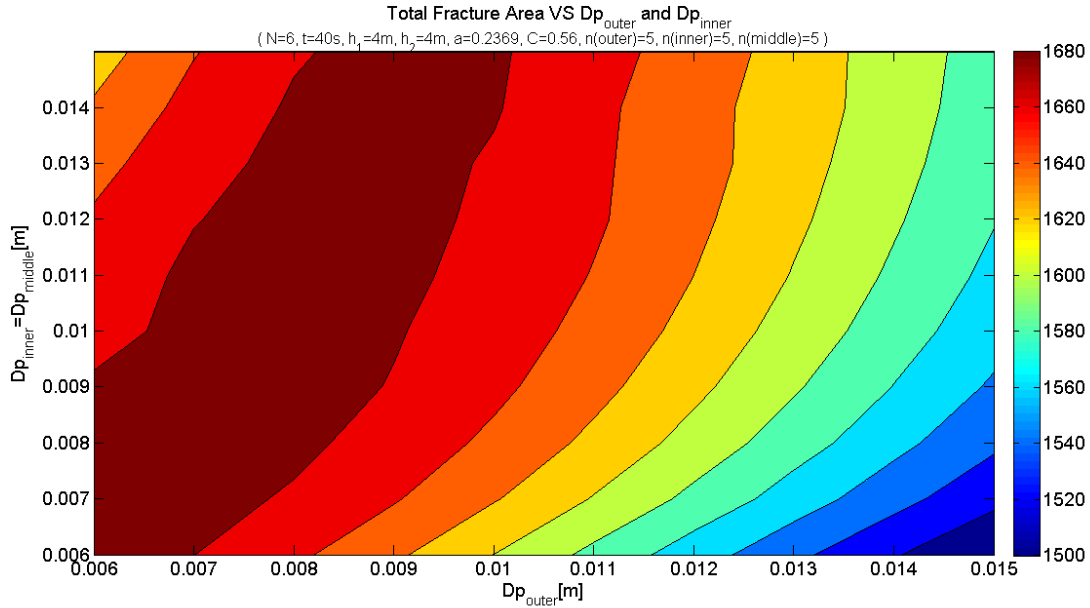


Figure 18. $A(t, h_1, h_2)$ vary with different Dp for constant n at uniform spacing.

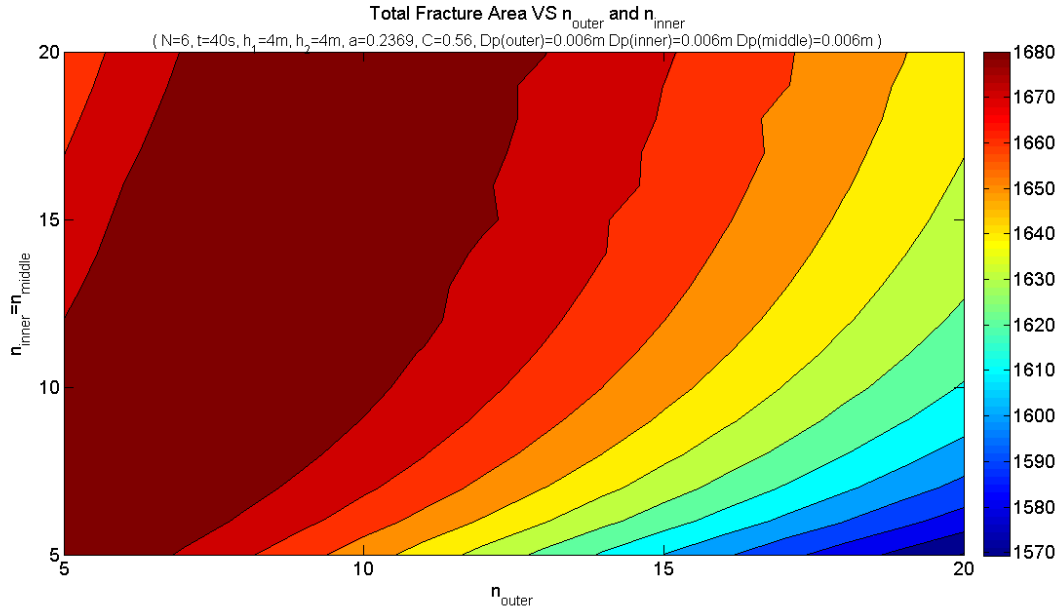


Figure 19. $A(t, h_1, h_2)$ vary with different n for constant Dp at uniform spacing.

To show difference between optimized and non-optimized design intuitively, we make the optimized design as $Dp(outer)=0.009m$, $Dp(inner)=0.015$, $Dp(middle)=0.015m$, $n(outer)=10$, $n(inner)=20$, $n(middle)=20$ and the non-optimized design as $Dp(outer)=0.015m$, $Dp(inner)=0.006m$, $Dp(middle)=0.006m$, $n(outer)=20$, $n(inner)=5$, $n(middle)=5$ from Figure 18 and 19. We find that 15% more fracture area is achieved by the optimized design (Figure 20). Figure 21 depicts a radius difference decrease by limited entry, which corresponds to a weaker stress shadow effect.

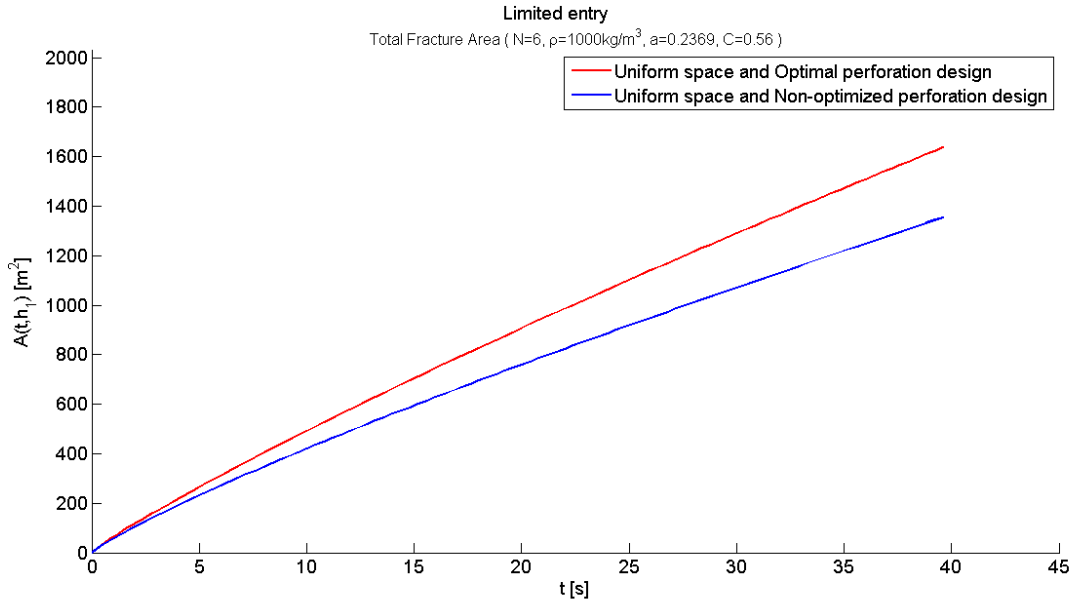


Figure 20. Area of optimized entry design compare with non-optimized at the uniform spacing.

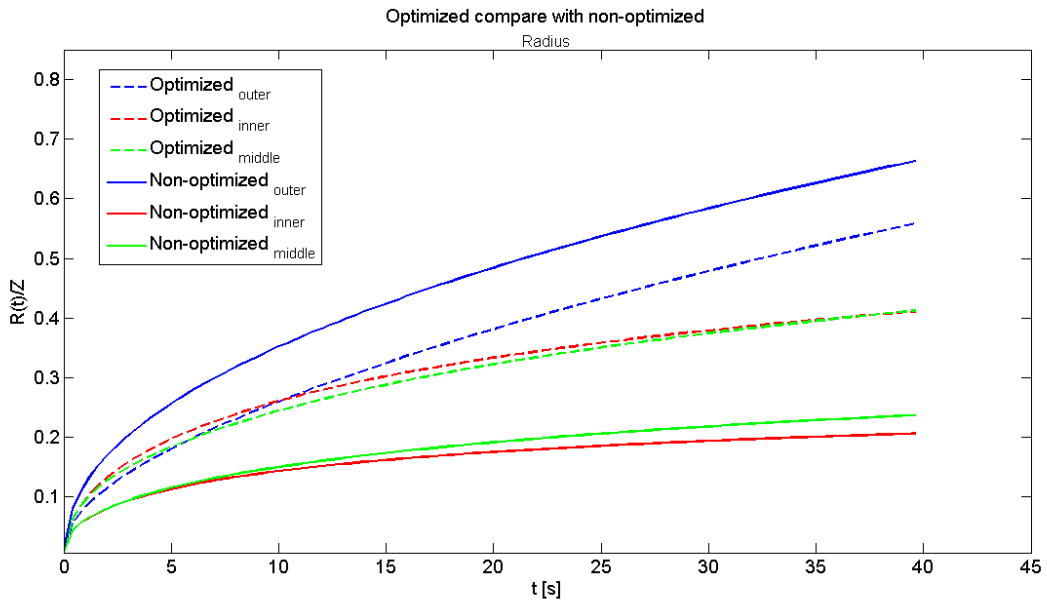


Figure 21. Radius of optimized entry design compare with non-optimized at the uniform spacing.

Whether considering five fractures or six fractures, larger Dp and n for inner fractures and middle fractures lead to greater fracture areas when using uniform spacing. But this non-uniform perforation case is not strictly the best limited entry design; $n=5$ and $Dp=0.006$ of every cluster can bring a little more fracture area, Figure 22. Because of the simplicity of the uniform limited entry design and uncertainty around limited entry design in general due to perforation erosion or plugging as the treatment progresses, the uniform perforation design has operational advantages over the more complicated non-uniform perforation limited entry design.

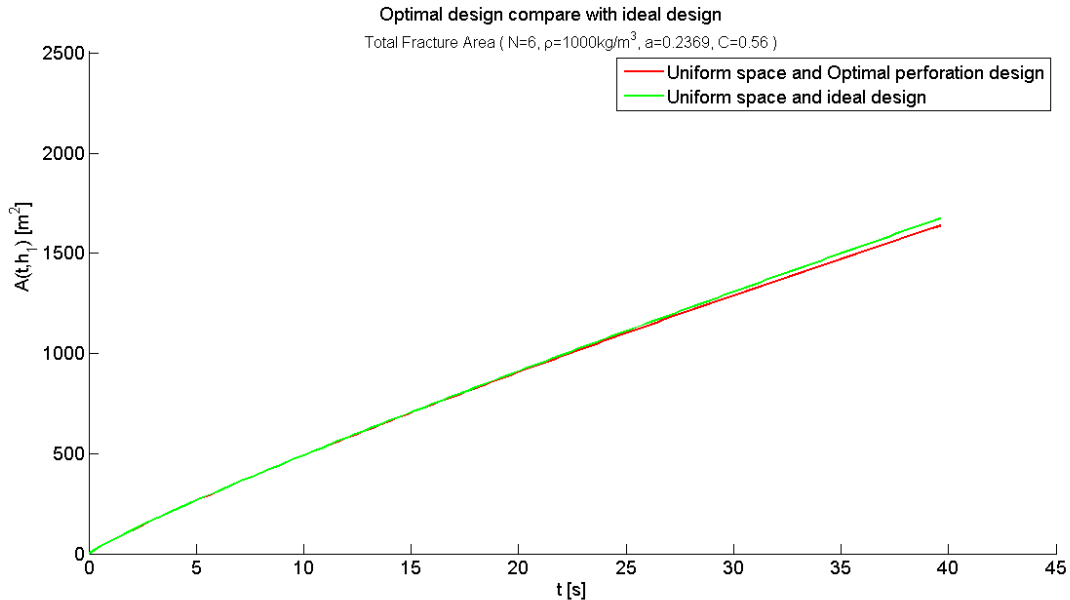


Figure 22. Area of optimized entry design compare with ideal design at the uniform spacing.

6.0 CONCLUSION

We built the C2Frac model to simulate how inter-fracture mechanical interactions effect the simultaneous development of hydraulic fractures from multiple perforations in a single stage. The benchmark ILSA model utilizes a novel parallel-planar 3D model incorporating full elastic-hydrodynamic coupling to account for the interaction effects. The C2Frac model, which is based on accounting for coupling among interacting fractures via a global energy balance relationship, achieves rapid computations as it utilizes a local integral approximation and asymptotic solutions to examine interference during the fracturing process. For the same numerical experiment, the C2Frac simulation requires only seconds to provide results while the ILSA model requires weeks.

When the spacing between fractures is uniform, the model confirms the phenomenon of stress shadowing in which growth of one or more fractures is suppressed by the stresses generated by their neighbors. However, we have also shown that by moving the location of inner fractures, it is possible to interfere with the localization process in a way that substantially changes the dynamics of the mutual interactions between the fractures. We determined there is the potential to increase the total fractured area in the array after 50 seconds of pumping by 7% compared to the uniform array by design $h_I=3.07\text{m}$. There is also an observed trend of increased benefit of the optimal spacing as time goes on, but because of the approximations it uses, C2Frac

cannot continue beyond the point where the radius of the largest fracture is more than 0.6 times the length of the fracture array (stage).

Non-uniform spacing is one way to stimulate all hydraulic fractures to grow simultaneously as far as possible. From our study, perforation-friction entry is shown to be a complimentary approach, minimizing the stress shadow effect by properly designing the perforation diameter and number. Power estimate, local integral and asymptotic solution are the methods C2Frac model based on to simulate the relationships between perforation pressure drop effect and stress shadow effect. The numerical experiment is distributed into uniform and non-uniform designs. Uniform corresponds to designs in which all clusters have same number of perforations and the same perforation diameter. Other designs are considered non-uniform. After comparing the two designs, we concluded that by choosing smaller perforation diameter and number for the outer cluster, the optimized spacing is closer to uniform at a given treatment time. In addition, such a design generates more fracture area at the uniform spacing. This improvement will increase with time. For a uniform five cluster design, we assigned 5 perforations with 6mm diameter for the outer cluster and 20 perforations with 15mm for the inner and middle clusters. At a treatment time of 25 seconds, optimal design created 50m^3 more fracture area than non-optimized. Such advantages amplify while time increases. From treat time 25 to 50 seconds, the divergence increases from 50m^3 to 100m^3 . The results can be used to design perforations number and diameter for different cluster to promote more fracturing area at a given perforation spacing. In the end, we combine the optimal perforation design with limited entry design to get the ultimate optimal design.

Future work will firstly be aimed at extended the range of time for which the approximations can be applied by using near-field approximations to the elastic interactions and by including the transition to blade-like fracture growth when/if the radial fractures are limited in

growth due to barriers above and below the reservoir. Future work will also focus on including fluid leakoff, proppant transport, and connecting the solutions with approximate reservoir simulators. Future work will also be aimed at testing the modeling and design with laboratory and field experiments.

BIBLIOGRAPHY

1. Abass HH. Soliman MY. Tahini AM. Surjaatmadja J. Meadows DL. and Sierra L. Oriented fracturing: A new technique to hydraulically fracture an openhole horizontal well. In Proceedings SPE Annual Technical Conference and Exhibition. New Orleans, LA, USA. SPE 124483. 2009.
2. Adachi J. Fluid-Driven Fracture in Permeable Rock. PhD thesis, University of Minnesota, Minneapolis, MN, 2001.
3. Baihly JD. Malpani R. Edwards C. Han SY. Kok JCL. Tollefsen EM. and Wheeler CW. Unlocking the shale mystery: How lateral measurements and well placement impact completions and resultant production. In Proceedings SPE Tight Gas Completions Conference. San Antonio, Texas, USA. SPE 138427. 2010.
4. Bungler AP. Analysis of the power input needed to propagate multiple hydraulic fractures. *International Journal of Solids and Structures* 50 (2013) 1538–1549. 2013.
5. Bungler AP. Jeffrey RG. Zhang X. Constraints on Simultaneous Growth of Hydraulic Fractures from Multiple Perforation Clusters in Horizontal Wells. SPE Hydraulic Fracturing Technology Conference held in The Woodlands, Texas, USA, 4–6 February 2013.
6. Cipolla C. Weng X. Onda H. Nadaraja T. Ganguly U. and Malpani R. New algorithms and integrated workflow for tight gas and shale completions. In Proceedings SPE Annual Technology Conference and Exhibition. Denver, Colorado, USA. SPE 146872. 2011.
7. Crump JB. and Conway MW. Effects of perforation-entry friction on bottomhole treating analysis. *J. Pet. Tech*, pages 1041–1049, 1988. SPE 15474.

8. Economides, M. and Nolte, K.G. 2000. Reservoir Stimulation, 3rd edition, New York: John Wiley & Sons, Ltd.
9. Fisher MK. Heinze JR. Harris CD. Davidson BM. Wright CA. and Dunn KP. Optimizing horizontal completion techniques in the Barnett shale using microseismic fracture mapping. In Proceedings SPE Annual Technology Conference and Exhibition. Houston, Texas, USA. SPE 90051. 2004.
10. Garagash D. Plane-strain propagation of a fluid driven fracture during injection and shut-in: Asymptotics of large toughness. ENG. FRACT. MECH. 73(2006)456-481.
11. Geertsma, J. and Klerk, F.d. 1969. A Rapid Method of Predicting Width and Extent of Hydraulically Induced Fractures. J. Pet. Tech. 21: 1571-1581.
12. Lecampion B. Desroches J. Simultaneous initiation of multiple transverse hydraulic fractures from a horizontal well. 48th US Rock Mechanics held in Minneapolis, MN, USA, 1-4 June. 2014.
12. Lecampion B. Desroches J. Can We Engineer Better Multistage Horizontal Completions? Evidence of the Importance of Near-Wellbore Fracture Geometry From Theory, Lab and Field Experiments. SPE Hydraulic Fracturing Technology Conference, The Woodlands, Texas, USA, 3-5 February, 2014.
14. Nordgren, R.P. 1972. Propagation of a Vertical Hydraulic Fracture. SPE. J. 12 (4): 306–314. SPE-3009-PA. <http://dx.doi.org/10.2118/3009-PA>.
15. Meyer B. Bazan L. A discrete fracture network model for hydraulically induced fractures-theory, parametric and case studies. In Proceedings SPE Hydraulic Fracturing Technology Conference and Exhibition. The Woodlands, Texas, USA. SPE 140514.6. 2011.
16. Miller C. Waters G. Rylander E. Evaluation of production log data from horizontal wells drilled in organic shales. In SPE North American Unconventional Gas Conference and Exhibition, The Woodlands, Tx, USA, 14-16 June 2011. SPE 144326. 2011.
17. Peirce AP. Bunger AP. Robustness of Interference Fractures that Promote Simultaneous Growth of Multiple Hydraulic Fractures. 48th US Rock Mechanics held in Minneapolis, MN, USA, 1-4 June. 2014.
18. Peirce A. Detournay E. An implicit level set method for modeling hydraulically driven fractures. Computer Meth. Appl. Mech. Eng. 197: 2858–2885. 2008.

19. Perkins, T.K. and Kern, L.R. 1961. Widths of Hydraulic Fractures. *J. Pet. Tech.* 13 (9): 937–949. SPE-89-PA. <http://dx.doi.org/10.2118/89-PA>.
20. Savitski AA. Detournay E. Propagation of a penny-shaped fluid-driven fracture in an impermeable rock: asymptotic solutions. *INT. J. SOLIDS. STRUCT.* 39 (2002) 6311–6337. 2002.